Table II. Histologic features of mobile and nonmobile plaques

Feature	*Mobile plaques (n = 18)*	*Nonmobile plaques (n = 17)*	P
Fibrous cap			
Plaque rupture, No. (%)	15 (83)	14 (82)	>.99
Minimum cap thickness, median (IQR) μm	80 (60-162.5)	100 (60-250)	.33
Fibrous cap area, median (IQR) μm^2	9200 (6300-13,100)	15,900 (9000-21,800)	.02
Mural thrombus, No. (%)	16 (89)	9 (59)	.06
Ratio of necrotic core area, mean (SD)	0.660 (0.098)	0.417 (0.176)	<.0001
Inflammation of fibrous cap, No. (%)			
Macrophages	17 (94)	16 (94)	1.00
Lymphocytes	12 (67)	12 (71)	1.00
Intraplaque hemorrhage, No. (%)			
Fresh	11 (61)	9 (53)	.74
Previous	11 (61)	10 (59)	1.00

IQR, Interquartile range; *SD,* standard deviation.

plaques in the prevalence of cap inflammation or intraplaque hemorrhage.

DISCUSSION

One of our results showed that progressive symptoms occurred more frequently in patients with mobile plaques than those with nonmobile plaques. This result is in line with unstable neurologic presentations depicted in previous case reports of symptomatic mobile plaques.[5,8] A recent study also concluded that the jellyfish sign, which is an ultrasonographic appearance of mobile plaques, was an important predictive factor for repeated ischemic stroke.[12] These findings, along with our results, promoted us to confirm the hypothesis that some histologic differences may exist between mobile and nonmobile plaques, even if both are symptomatic plaques.

There are several reports about mobile plaques in large arteries, including the carotid artery,[2-8,19,20] and some reports have described the histology of mobile plaques. Nakajima et al[5] reported the pathologic findings of a mobile plaque in the brachiocephalic artery that caused fatal recurrent strokes and pointed out that plaque disruption was a cause of the mobility. Arning et al[6] also found a mural thrombus in the histology of a mobile carotid plaque. Our results are compatible with previous pathologic reports about mobile plaques. However, the features of plaque rupture and mural thrombus may not be sufficient to describe the specific histopathology of a mobile plaque, because according to our result, the prevalence of plaque disruption or mural thrombus of mobile plaques is not significantly higher than that of nonmobile plaques. The findings of the present study suggest that the existence of a large, soft, lipid-rich necrotic core is also important for the mechanism of plaque mobility.

This speculation conforms with the results on intravascular ultrasound elastography, a recently developed technique to assess the elasticity of plaque tissue using intravascular ultrasound imaging by measuring the "strain" or small movement of plaque tissue under an applied force.[21,22] The authors of those studies demonstrated that the strain could distinguish lipid-rich components from hard and fibrous components. Mobile structures on carotid plaques may be caused not only by the mural thrombus formed by a fibrous cap rupture but also by a large, lipid-rich necrotic core exposed into the blood lumen.

Several pathologic reviews have reinforced the evidence that a large necrotic core is one of the important features of so-called vulnerable plaque.[23-27] Studies on aortic plaques,[28,29] an in vivo study on magnetic resonance imaging,[30] and histologic studies of carotid plaque[16,31] have also shown that a large necrotic core was strongly associated with thrombosis, fibrous cap rupture, fibrous cap thinning, or neurologic symptoms. Moreover, when the large lipid-rich necrotic core is exposed to blood lumen by plaque rupture, the mural thrombus or debris from the lipid core may become a persistent source of embolism, which may result in an unstable ischemic stroke. On the other hand, Redgrave et al[16] showed that thinning of the fibrous cap covering the necrotic core is another important factor for plaque vulnerability. These authors advocated critical cap thickness (minimum cap thickness <200 μm and a representative cap thickness <500 μm) as a marker for ruptured plaque.

Using these criteria, the fibrous cap of both groups in our study is extremely thin. One possible reason that we did not find a significant difference in minimum fibrous cap thickness in the two plaques is that mobile and nonmobile plaques had an almost equally high prevalence of cap rupture. Given that the actual fibrous cap area was smaller in mobile plaques than in nonmobile plaques (Table II), it is possible that the overall thickness of fibrous caps in mobile plaques is smaller than that in nonmobile plaques.

To our knowledge, only one recent study demonstrated the histologic features of mobile carotid plaques, although it did not include a controlled group in histologic assessment. Kume et al[12] examined histologic features of 15 plaques with ultrasonographic jellyfish sign, and the results showed that the proportional area of the fibrous cap correlated negatively with jellyfish-positive plaque surface movement rate. Our results regarding the fibrous cap area

coincides with their results. They could not, however, document significant correlation between atheromatous lesion area and the plaque motion rate, which is inconsistent with our results. This may be attributed to the differences in a patient population, in definitions of ultrasonographic and histopathologic findings, and in research designs between the two studies. The large necrotic core can still be one of the representative features of mobile plaques because the present results were conducted in a controlled study.

Our study has some limitations. First, the number of the cases we studied was small, and not all of the nonmobile plaques were examined. Larger studies are necessary to confirm higher prevalence of mural thrombus and thinner fibrous cap in mobile plaques.

Second, because nonmobile plaques had a longer duration until CEA, stabilization of the plaque, which can occur within approximately 90 days after the presenting neurologic symptom,[31,32] could have led us to underestimate some of the histologic factors of nonmobile plaques. However, one study showed that the prevalence of a large lipid core and mural thrombus was not influenced by the span of time since the last ischemic events.[31] Spagnoli et al[33] also revealed that a fresh thrombus can present several months after the first cerebrovascular event.

Third, we only studied symptomatic plaques and did not include asymptomatic plaques. Our study, therefore, did not answer the question of whether mobile plaques are more "vulnerable" than nonmobile plaques as long as the word "vulnerable" means the tendency for fibrous cap rupture and the potential of subsequent embolic stroke. That was not, however, the purpose of this study. Further studies including both symptomatic and asymptomatic patients might be essential to determining whether mobile plaques are more "vulnerable" than nonmobile plaques.

A higher prevalence of mobile plaques is shown in this report (9.3% of excised plaque) than in previous study.[1] The most recent study demonstrated an even higher prevalence (19%) of mobile plaques.[12] This high prevalence of mobile plaques may be explained by the evolution of the duplex ultrasound imaging system and sheds light on the clinical importance of mobile plaques.

CONCLUSIONS

In this study, we have clarified the histologic difference between mobile and nonmobile symptomatic carotid plaques. This result may partly explain unstable neurologic presentations of patients with mobile carotid plaques and may add information to the debate regarding the management of mobile plaques. Further studies on the histopathology and natural history of the mobile carotid plaque are needed to establish the most effective acute management for symptomatic mobile plaques.

We especially appreciate Dr Kimitoshi Satou for helpful advice on the study design. We also wish to thank Sumiko Matsushima and Laura Dickinson for preparing this manuscript, and Toshie Urano and Mayumi Oka for collecting patient records.

AUTHOR CONTRIBUTIONS

Conception and design: TF, KI
Analysis and interpretation: TF, KN, HI
Data collection: TF, KN, TH
Writing the article: TF
Critical revision of the article: KI, SM
Final approval of the article: KI, HI
Statistical analysis: TF
Obtained funding: Not applicable
Overall responsibility: TF

REFERENCES

1. Szendro G, Sabetai MM, Tegos TJ, Dhanjil S, Lennox AF, Nicolaides AN. Mobile carotid plaques: the natural history of two asymptomatic and non-operated cases. J Vasc Surg 1999;30:357-62.
2. Cho YP, Kwon TW, Kim GE. Sonographic appearance of a free-floating atheromatous plaque in a patient with acute stroke. J Clin Ultrasound 2002;30:317-21.
3. Ferrero E, Gaggiano A, Ferri M, Nessi F. Mobile floating carotid plaque post-trauma. Diagnosis and treatment. Interact Cardiovasc Thorac Surg 2009;8:496-7.
4. Ko PT, Lin SK, Chang YJ, Ryu SJ, Chu CC. Carotid floating plaques associated with multiple cerebral embolic strokes. Case reports. Angiology 1997;48:255-61.
5. Nakajima M, Yasaka M, Minematsu K. Mobile thrombus from a ruptured plaque in the brachiocephalic artery. J Stroke Cerebrovasc Dis 2008;17:423-5.
6. Arning C, Herrmann HD. Floating thrombus in the internal carotid artery disclosed by B-mode ultrasonography. J Neurol 1988;235:425-7.
7. Combe J, Poinsard P, Besancenot J, Camelot G, Cattin F, Bonneville JF, et al. Free-floating thrombus of the extracranial internal carotid artery. Ann Vasc Surg 1990;4:558-62.
8. Choukroun EM, Labrousse LM, Madonna FP, Deville C. Mobile thrombus of the thoracic aorta: diagnosis and treatment in 9 cases. Ann Vasc Surg 2002;16:714-22.
9. Di Tullio MR, Russo C, Jin Z, Sacco RL, Mohr JP, Homma S. Aortic arch plaques and risk of recurrent stroke and death. Circulation 2009; 119:2376-82.
10. Ay H, Koroshetz WJ, Benner T, Vangel MG, Wu O, Schwamm LH, et al. Transient ischemic attack with infarction: a unique syndrome? Ann Neurol 2005;57:679-86.
11. Fox AJ. How to measure carotid stenosis. Radiology 1993;186:316-8.
12. Kume S, Hama S, Yamane K, Wada S, Nishida T, Kurisu K. Vulnerable carotid arterial plaque causing repeated ischemic stroke can be detected with B-mode ultrasonography as a mobile component: jellyfish sign. Neurosurg Rev 2010;33:419-30.
13. Alers JC, Krijtenburg PJ, Vissers KJ, van Dekken H. Effect of bone decalcification procedures on DNA in situ hybridization and comparative genomic hybridization. EDTA is highly preferable to a routinely used acid decalcifier. J Histochem Cytochem 1999;47:703-10.
14. Bassiouny HS, Davis H, Massawa N, Gewertz BL, Glagov S, Zarins CK. Critical carotid stenoses: morphologic and chemical similarity between symptomatic and asymptomatic plaques. J Vasc Surg 1989;9:202-12.
15. Kolodgie FD, Gold HK, Burke AP, Fowler DR, Kruth HS, Weber DK, et al. Intraplaque hemorrhage and progression of coronary atheroma. N Engl J Med 2003;349:2316-25.
16. Redgrave JN, Gallagher P, Lovett JK, Rothwell PM. Critical cap thickness and rupture in symptomatic carotid plaques: the Oxford plaque study. Stroke 2008;39:1722-9.
17. Lovett JK, Gallagher PJ, Rothwell PM. Reproducibility of histological assessment of carotid plaque: implications for studies of carotid imaging. Cerebrovasc Dis 2004;18:117-23.
18. Bassiouny HS, Sakaguchi Y, Mikucki SA, McKinsey JF, Piano G, Gewertz BL, et al. Juxtalumenal location of plaque necrosis and neo-

formation in symptomatic carotid stenosis. J Vasc Surg 1997;26: 585-94.
19. Lozano P, Gomez FT, Julia J, M-Rimbau E, Garcia F. Recurrent embolism caused by floating thrombus in the thoracic aorta. Ann Vasc Surg 1998;12:609-11.
20. Mochizuki S, Takayama S, Nishiyama T, Kakizawa H, Shikaura K, Sakamoto M, et al. Two cases of protruding atherosclerotic plaque with mobile projections in the aortic arch. Intern Med 1993;32:777-80.
21. de Korte CL, Pasterkamp G, van der Steen AF, Woutman HA, Bom N. Characterization of plaque components with intravascular ultrasound elastography in human femoral and coronary arteries in vitro. Circulation 2000;102:617-23.
22. de Korte CL, Sierevogel MJ, Mastik F, Strijder C, Schaar JA, Velema E, et al. Identification of atherosclerotic plaque components with intravascular ultrasound elastography in vivo: a Yucatan pig study. Circulation 2002;105:1627-30.
23. Falk E. Stable versus unstable atherosclerosis: clinical aspects. Am Heart J 1999;138:S421-5.
24. Shah PK. Mechanisms of plaque vulnerability and rupture. J Am Coll Cardiol 2003;41:15S-22S.
25. Nighoghossian N, Derex L, Douek P. The vulnerable carotid artery plaque: current imaging methods and new perspectives. Stroke 2005; 36:2764-72.
26. Golledge J, Greenhalgh RM, Davies AH. The symptomatic carotid plaque. Stroke 2000;31:774-81.
27. Gutstein DE, Fuster V. Pathophysiology and clinical significance of atherosclerotic plaque rupture. Cardiovasc Res 1999;41:323-33.
28. Davies MJ, Richardson PD, Woolf N, Katz DR, Mann J. Risk of thrombosis in human atherosclerotic plaques: role of extracellular lipid, macrophage, and smooth muscle cell content. Br Heart J 1993;69: 377-81.
29. Felton CV, Crook D, Davies MJ, Oliver MF. Relation of plaque lipid composition and morphology to the stability of human aortic plaques. Arterioscler Thromb Vasc Biol 1997;17:1337-45.
30. Cappendijk VC, Kessels AG, Heeneman S, Cleutjens KB, Schurink GW, Welten RJ, et al. Comparison of lipid-rich necrotic core size in symptomatic and asymptomatic carotid atherosclerotic plaque: initial results. J Magn Reson Img 2008;27:1356-61.
31. Redgrave JN, Lovett JK, Gallagher PJ, Rothwell PM. Histological assessment of 526 symptomatic carotid plaques in relation to the nature and timing of ischemic symptoms: the Oxford plaque study. Circulation 2006;113:2320-8.
32. Russell DA, Wijeyaratne SM, Gough MJ. Changes in carotid plaque echomorphology with time since a neurologic event. J Vasc Surg 2007;45:367-72.
33. Spagnoli LG, Mauriello A, Sangiorgi G, Fratoni S, Bonanno E, Schwartz RS, et al. Extracranial thrombotically active carotid plaque as a risk factor for ischemic stroke. JAMA 2004;292:1845-52.

Submitted Aug 25, 2010; accepted Oct 18, 2010.

Additional material for this article may be found online at www.jvascsurg.org.

Evaluation of a Brain Imaging System with Combined Parallel Hole and Pinhole Collimation

Qiu Huang, Tsutomu Zeniya, Yoshiyuki Hirano, Hiroyuki Kudo, Hidehiro Iida, and Grant T. Gullberg

Abstract–This work evaluates the brain imaging system designed by the Department of Investigative Radiology at the National Cardiovascular Research Center- Research Institute in Osaka, Japan. As presented at the IEEE Nuclear Science Symposium and Medical Imaging Conference at Knoxville, TN in 2010, the high resolution single photon emission computed tomography (SPECT) imager was developed for obtaining high resolution brain scans for various imaging diagnostic applications. The system was mounted with one large field of view detector imaging the whole brain and multiple smaller field of view high resolution detectors imaging small regions of the brain. The large field of view detector provides images without truncation that localize areas of particular diagnostic interest and provide support information for the reconstruction of high resolution regions of interest (ROIs) from high resolution truncated projections obtained with the small field of view detectors. At the IEEE conference, the authors suggested a geometry which achieved high resolution reconstruction of the brain with a small pinhole aperture. The work presented in this paper simulates the camera with larger pinholes and shows that the camera has accurate quantitation and fine resolution for the interior reconstruction problem.

I. INTRODUCTION

SPECT plays an active role in brain imaging. For example, in clinical evaluation for diagnosing brain autoregulatory abnormalities, cerebral blood flow (CBF) and cerebral vascular reactivity (CVR) is quantified in a single session using a split dose administration of ^{123}I-iodo-amphetamine (IMP); one at rest and one during Diamox challenge. In addition, to evaluate neuronal damage due to ischemia and to provide prognostic value for surgical outcomes, Iodine-123-iomazenil (Iomazenil) is used to image the binding to benzodiazepine receptors prior to carotid endoarterectomy. To better quantify the brain function, the Department of Investigative Radiology at the National Cardiovascular Research Center - Research Institute in Osaka, Japan is designing a high resolution single photon emission computed tomography (SPECT) imager as shown in Fig. 1 for obtaining high resolution brain images. The camera consists of one large field of view detector imaging the whole brain and multiple smaller field of view high resolution detectors imaging small regions of the brain. The observed intrinsic spatial resolution of the large FOV detector in the x and y-direction are 3.5 mm and 3.1 mm, respectively. The intrinsic spatial resolution of the small FOV detector in the x and y-direction and the energy resolution are 2.3 mm, 2.4 mm, and 6.1 %, respectively [1].

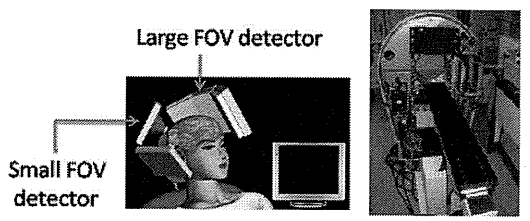

Figure 1. Camera with large field of view detector for imaging whole brain and smaller field of view detectors for imaging ROIs (left), and the prototype system (right).

The large field of view detector provides images without truncation that localize areas of particular diagnostic interest and provides support information for the reconstruction of high resolution regions of interest (ROIs) from high resolution truncated projections obtained with the small field of view detectors. The work presented in this paper provides simulations which show that the camera improves the quantitation for the interior reconstruction problem with a few multiple pinhole collimated detectors.

The pinhole collimator is able to achieve higher geometric resolution than a parallel-hole collimator. In addition, at a small object-to-detector distance, sensitivity of pinholes can be higher than that of the parallel-hole collimator [2]. However, the advantage is guaranteed at the expense of a smaller field of view, which results in truncated projections. The reconstruction of these projections involves determining the solution to the interior problem in local tomography. The interior problem in medical imaging refers to the

Manuscript received November 21, 2010. This work was supported by NIH under Grant No.R01EB00121, by the Director, Office of Science, Office of Biological and Environmental Research of the US Department of Energy under contract DE-AC02-05CH11231, by the Grant for Translational Research from the Ministry of Health, Labour and Welfare (MHLW), Japan, and by the Specialized Research Fund for the Doctoral Program of Higher Education (SRFDP), China, Grant No. 20100073120003.

Q. Huang is with the Shanghai Jiao Tong University, Shanghai, China (e-mail: huangjone@yahoo.com).

T. Zeniya, Y. Hirano and H. Iida are with the National Cardiovascular Center Research Institute, Suita, Osaka, Japan.

H. Kudo is with University of Tsukuba, Tsukuba, Japan.

G. T. Gullberg is with the Lawrence Berkeley National Laboratory, Berkeley, CA USA.

situation where the region-of-interest (ROI) is totally contained within the object. For instance, in SPECT, the interior problem happens when the projections passing through the region outside the ROI are truncated due to a small field-of-view detector or a short detector-to-object distance in the case of converging collimation. The interior problem has been studied for some time [3]. Recently, it was proven that the solution is unique and stable in computed tomography (CT) if a small region in the ROI is known *a priori* [4-9]. In this paper, the SPECT interior reconstruction problem is solved using an iterative algorithm as presented in [10].

To further increase the sensitivity of the system, the small FOV detector is mounted with multiple pinhole collimators. The pinhole apertures are chosen to be 2mm instead of 0.5mm in the previous work [10]. Stationary small FOV detectors are simulated to acquire data assuming the region of interest is at the center of the brain or at the posterior region of the brain.

The paper is organized as follows: Section II shows the method we used to simulate the combined parallel-hole and pinhole collimated imager and the algorithm to reconstruct the pinhole data. The result of a numerical simulation is presented in Section III where comparisons are made to illustrate the resolution and quantification of the camera. Then the conclusion is given in Section IV.

II. Methods

We performed a simulation study using the digital XCAT brain phantom [11]. The phantom was stored in a 3-dimensional volume with each voxel being $(2\text{mm})^3$. One slice of the phantom is shown in Fig. 2.

The large field of view parallel-hole collimated detector was simulated to revolve around the brain and acquire data every 5 degrees over half a circle. The detector bin was 0.28 cm along the transversal direction and 0.2 cm along the axial direction. Poisson noise was manually added to the data to give a noise level such that the total counts of each slice summed to 10^7. The filtered backprojection algorithm was applied to the simulated projection data to reconstruct a volumetric image. Fig. 3 gives an example of one slice of the reconstructed low resolution parallel data. The image was interpolated and smoothed and was later used as the initial image and as prior information in the reconstruction of the pinhole data. A mask image was also generated according to the reconstructed image from data acquired with large FOV parallel-hole collimated detectors, which was later used in the iterative reconstruction of data for the small FOV pinhole collimated detectors.

Fig. 2. The original XCAT phantom.

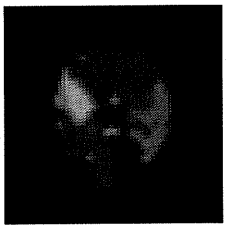

Fig. 3. The reconstructed image from parallel-hole projection data.

The pinhole collimator is shown in Fig. 4. It had a circular aperture with a radius of 2 mm and a knife edge with an opening angle of $\pi/3$.

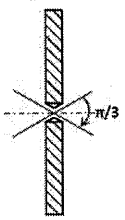

Fig. 4. The pinhole collimator. The pinhole is a circular aperture with a radius of 2mm and a knife edge with an opening angle of $\pi/3$.

In each small FOV detector, 3×3 pinholes were attached all focusing to common point, which could be the center of rotation though the detectors are stationary during data acquisitions. The view of the pinhole plane is shown in Fig. 5(a). Each pinhole is separated from the other by 5.5 mm both in the horizontal and vertical directions. The side view in Fig. 5(b) shows the geometry simulated in this work, which gives a magnification factor of 1.

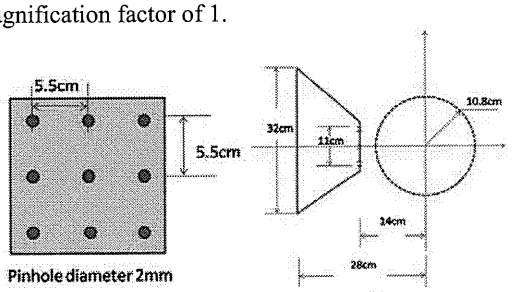

(a) (b)

Fig. 5. Side view and top view of the multiple pinhole collimator. The plane with 3×3 pinholes (a), The side view of one detector head with the multiple pinhole collimation.

The small FOV detectors used a 2×2 H8500 PMT block for each pinhole. The 10×10 cm^2 blocks were connected with a 1cm septa in between to avoid overlap between projections through adjacent pinholes. The detector plane is illustrated in Fig. 6. The 2D detector plane had an area of 32×32 cm^2.

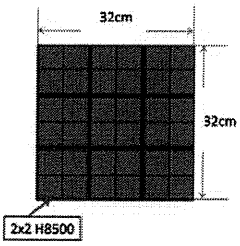

Fig. 6. The detector plane for a 3×3 pinhole collimator. Each pinhole is mounted with a 2×2 H8500 PMT block.

Four small FOV detectors were then localized close to the object as shown in Fig. 7. The FOV is then a sphere with a radius of 5mm. In other words, the projections were truncated. One view is shown in Fig. 8. In the figure, the detector bin is 2 mm.

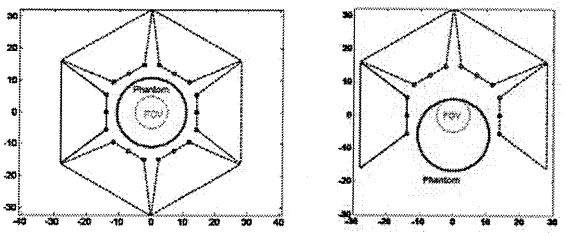

Fig. 7. The two geometries simulated in this work.

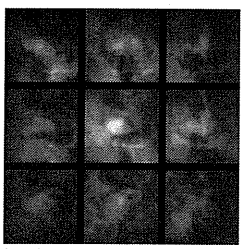

Fig. 8. The projection at one view of the 6 views for the geometry on the left shown in Fig. 7.

The reconstruction algorithm was developed to maximize *a posteriori* probability of the image given the simulated projections. Details could be found in [10].

III. Results

There are two geometries simulated in this work for the small FOV detectors: first one with 6 detector heads and the second with 4 detector heads, as shown in Fig. 7. In addition to the XCAT phantom, a point source phantom was also used to evaluate the system resolution.

The study with the XCAT phantom is shown in Fig. 9. The reconstructed images are from the geometry with 6 and 4 projection views, respectively. Profiles are plotted in Fig. 10 to show that the two geometries both improve the details in the reconstructed images over that obtained with the parallel-hole collimated detector. For the geometry with 6 views, the FOV is located at the center of the brain. While for the geometry with 4 views, the FOV is located at the posterior region of the brain. Both FOVs were reconstructed with higher resolution compared to the reconstruction shown in Fig. 3. Another comparison was performed with the point source phantom.

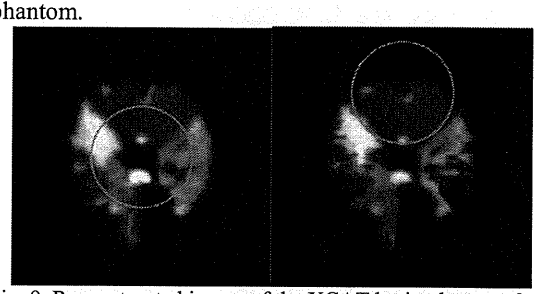

Fig. 9. Reconstructed image of the XCAT brain phantom from pinhole data for the interior problem and for limited angular sampling. MAP estimate with regularization is applied, for the geometry with 6 views (left) and for the geometry with 4 views (right). The circle on the image indicates the FOV.

In the simulation, the pinhole data were acquired with truncation, resulting in reconstructing an interior problem. Efforts should be made to correct for the effect of this problem. In this work, we used the low resolution image obtained by the large field of view detector first as the initial estimate in the iterative reconstruction of the pinhole data. Also, the low resolution image provided a priori information and a mask for the reconstruction of the interior problem. The prior information was used to calculate the L2 norm distance from the reconstructed image to compose the penalty term in addition to the total variation regularization. The image quality within the FOV, which was the central part of the brain for the geometry with 6 views and the posterior region of the brain for the geometry with 4 views, was improved.

The vertical and horizontal profiles crossing the FOV are shown in Fig. 10. From the profiles we see that the details of the image are more distinct by reconstructing both parallel-hole projection data and pinhole projection data; for instance, the details indicated by the arrows in Fig. 10.

The study with point source phantom is shown in Fig. 11 for the geometry with 6 views. In the reconstruction, no prior information was used, however the total variation regularization was used in the iteration. The image shows that the resolution of the system is fairly good. Although with the truncation problem, the quantification is degraded.

Profiles for the three points labeled in Fig. 11 with the three arrows are drawn in Fig. 12. The dash lines (red) indicate the original phantom, and the solid lines (blue) are for the reconstructed images. The profiles imply high resolution for the system, however, with degradation of

quantitation for points off the FOV, for example, points 1 and 3.

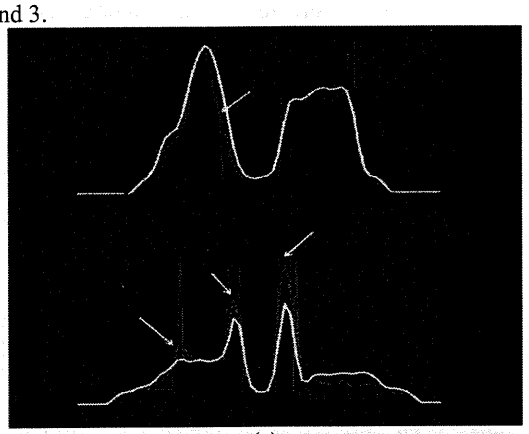

(a)

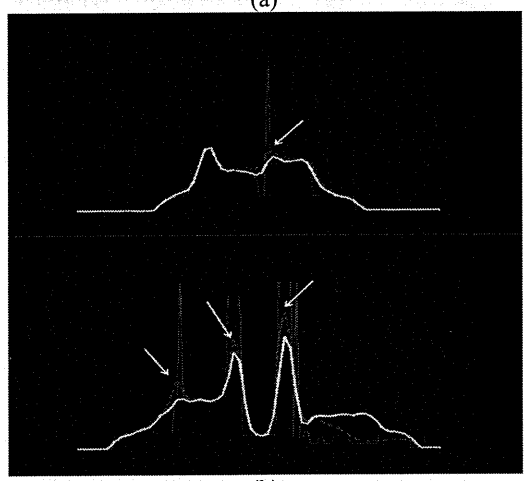

(b)

Fig. 10. Horizontal and vertical profiles crossing the center of the FOV for the geometry with 6 views (a) and for the geometry with 4 views (b). The purple solid line (thin) indicates the original phantom. The yellow dot-dash line is for the reconstructed image (Fig. 3.) from parallel-hole collimated data. While the red solid line (thick) is for the reconstructed image in Fig. 9.

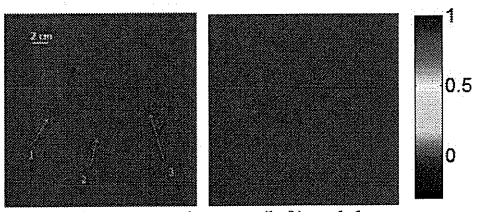

Fig. 11. Point source phantom (left) and the reconstructed image of the point source phantom for the geometry with 6 views (right).

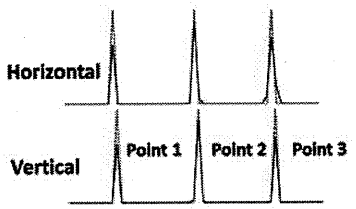

Fig. 11. The horizontal and vertical profiles for lines passing through the three points indicated in Fig. 11.

IV. Conclusion

The combination of a large field of view parallel-hole collimated detector and smaller field of view high resolution pinhole detectors improves the quantitation in simulated brain imaging. It makes use of the high sensitivity of the pinhole collimator while compensates for the degradation in the reconstructed image due to the interior reconstruction problem caused by the small field of view of the pinhole collimator. This work will be verified through phantom imaging studies.

References

[1] Y. Hirano, T. Zeniya, and H. Iida, "Development of a high resolution and quantitative SPECT for the human brain," *IEEE Nuclear Science Symposium and Medical Imaging Conference*, Knoxville, TN, 2010.

[2] R. J. Jaszczak, J. Li, H. Wang, M. R. Zalutsky, and R. E. Coleman, "Pinhole collimation for ultra-high-resolution, small-field-of-view SPECT," *Phys. Med. Biol.*, vol. 39, pp. 425-437, 1994.

[3] F. Natterer, *The Mathematics of Computerized Tomography* (SIAM), 1986.

[4] G. Wang, Y. Ye and H. Yu, "General VOI/ROI reconstruction methods and systems using a truncated Hilbert transform," Patent disclosure submitted to Virginia Tech. Intellectual Properties on May 15 2007.

[5] Y. Ye, H. Yu, and G. Wang, "Exact interior reconstruction with cone-beam CT," *Int. J. Biomed. Imaging,* Article ID. 10693, 2007.

[6] Y. Ye, H. Yu, Y. We and G. Wang, "A general local reconstruction approach based on a truncated Hilbert transform," *Int. J. Biomed. Imaging*, Article ID. 63634, 2007.

[7] Y. Ye, H. Yu, and G. Wang, "Exact interior reconstruction from truncated limited-angle projection data," *Int. J. Biomed. Imaging*, Article ID. 427987, 2008.

[8] M. Courdurier, F. Noo, M. Defrise and H. Kudo, "Solving the interior problem of computed tomography using a priori knowledge," *Inverse Problems*, vol. 24, pp. 065001, 2008.

[9] H. Kudo, M. Courdurier, F. Noo, and M. Defrise, "Tiny a proiri knowledge solves the interior problem in computed tomography," *Phys. Med. Bio.*, vol. 53, pp. 2207-2231, 2008.

[10] Q. Huang, T. Zeniya, H. Kudo, H. Iida, and G. T. Gullberg, "High resolution brain imaging with combined parallel hole and pinhole collimation," *IEEE Nuclear Science Symposium and Medical Imaging Conference*, Knoxville, TN, 2010.

[11] W. P. Segars and B. M. W. Tsui, "MCAT to XCAT: the evaluation of 4-D computerized phantoms for imaging research," *Proceedings of the IEEE*, vol. 97, No. 12, 2009.

Towards a High-Resolution Local Tomography Using Statistical Iterative Reconstruction

Essam A. Rashed, *Member, IEEE,* Hiroyuki Toda, Toshihiro Sera, Akira Tsuchiyama, Tsukasa Nakano, Kentaro Uesugi and Hiroyuki Kudo, *Member, IEEE*

***Abstract*—Synchrotron radiation (SR) x-ray micro-CT is an effective method for high-resolution imaging of small objects with several applications in biology and industry. However, the detector field of view is tiny, which limits the sample size to a few millimeters. When the sample size is larger than the limited field of view, reconstructed images, using conventional methods, known to suffer from DC-shift and low-frequency artifacts. This problem is known as local tomography or interior problem. In this paper we introduce a statistical iterative image reconstruction method to eliminate image artifacts produced from local tomography. The proposed method can be used in several SR imaging applications to enable a high resolution of the scanned object while preserving the image quality from artifacts produced due to the local tomography problem.**

I. Introduction

Synchrotron radiation (SR) micro-CT systems that provide a high-resolution cross-sectional images of small animals and other applications had a strong impact in several research fields such as drug developments. To obtain high-resolution CT images, it is required that the object is located completely inside the detector field of view (FOV). However, in many cases, a portion of the scanned object lies outside the FOV which leads to a truncation in the acquired projection data. Data truncation may also occur due to the magnification of a specific portion of the object or to reduce unnecessary radiation to the remaining portion of the object (Fig. 1). The most sever truncation case is when the projection data is truncated in all view angles providing the so-called local tomography or the interior problem [1]. It is known that when the projection data is fully truncated such as the case of local CT imaging, the reconstructed images suffers from DC-shift (or cupping) and low-frequency artifacts. These artifacts become strong in regions close to the boundaries of the FOV. The local tomography is also known as an ill-posed inverse problem which had been studied for a long time. Based on the analytical reconstruction, it was believed that all projection rays passing through the whole object are required for exact reconstruction and any truncation leads to losing the solution exactness. However, the recently developed theories based on the concept of Differentiated Backprojection (DBP) [2]–[4] and Backprojection-Filtration (BPF) [5] succeeded in reducing the required set of projection rays for theoretically exact and stable reconstruction.

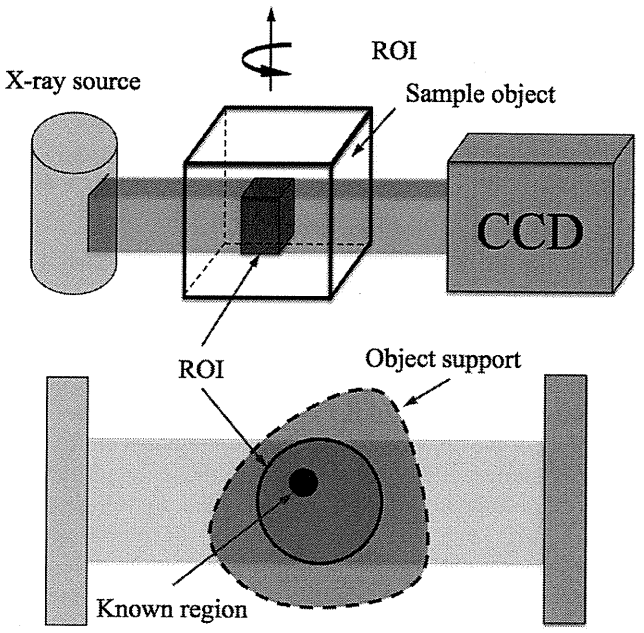

Fig. 1. Local tomography in SR micro-CT. The sample object usually extend outside the FOV of the CCD used for data acquisition. For accurate reconstruction, it required to know the object contour line (object support in additional to a region inside the region of interest (ROI).

In our earlier work, we proposed a statistical iterative reconstruction algorithm for region-of-interest (ROI) reconstruction when the projection data is partially truncated [6]. Here, we extend this algorithm to the case of local tomography. Experimental results using real data obtained from high-resolution SR imaging indicates a significant reduction in the image artifacts when the proposed method is used.

II. Proposed Method

A. Object support constraint

According to the theories based on the analytical concept of Hilbert transform in [3], [4], [7], it is possible to reconstruct exact image from locally truncated data if the following constrains are satisfied. 1) All projection rays passing through

This work was partially supported by Grant-in-Aid from the Japan Society for the Promotion of Science (JSPS). Grant for foreign post-doctoral fellows (ID No. P10052).

E.A.Rashed and H.Kudo are with the Department of Computer Science, Graduate School of Systems and Information Engineering, University of Tsukuba, Tsukuba 305-8573, Japan. H.Toda is with the Toyohashi University of Technology, Toyohashi, Japan, T.Sera and A.Tsuchiyama are with the Osaka University, Osaka, Japan. T.Nakano is with the AIST, Tsukuba, Japan. K.Uesugi is with the Japan Synchrotron Radiation Research Institute, Hyogo, Japan. E.A.Rashed is also with the Department of Mathematics, Faculty of Science, Suez Canal University, Ismailia 41522, Egypt (e-mail: essam@imagelab.cs.tsukuba.ac.jp).

978-1-4673-0119-0/11/$26.00 ©2011 IEEE

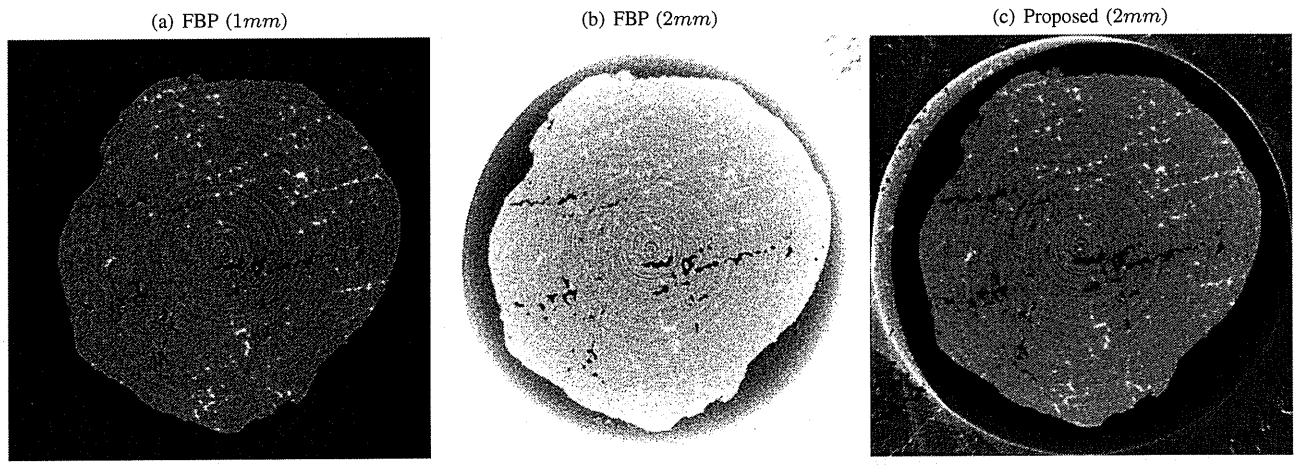

Fig. 2. Image reconstruction for the Aluminum alloy data. (a) Image reconstructed using FBP method from non-truncated data, to be used as true reference. Images reconstructed from local data using FBP algorithm in (b) and proposed method in (c).

FOV are included in the measured projection data, 2) a compact support of the object is available, 3) *a priori* known information of intensity value for small region inside the FOV is available, and 4) for iterative reconstruction, the image matrix should be large enough to include the entire object. The second constraint is not always available, as the exact definition of the object contour requires additional efforts such as extra hardware. The iterative reconstruction algorithm for ROI reconstruction (ROI-OSEM), detailed in [6], provides an automatic and efficient detection of the object support in parallel to the image reconstruction. In the following, we review the main approach of the ROI-OSEM algorithm with modifications that suits the correct noise modeling in transmission CT:

B. Iterative reconstruction algorithm

We consider the following noise model:

$$y_i \approx \text{Poisson}\ [b_i \exp(-\langle \vec{a_i}, \vec{x} \rangle)] \tag{1}$$

where $\vec{x} = (x_1, \ldots, x_n)^\top$ is the image vector, $\vec{y} = (y_1, \ldots, y_m)^\top$ be the measured counts, $\vec{b} = (b_1, \ldots, b_m)$ is the blank scan, $A = \{a_{ij}\}$ is the $m \times n$ system matrix and $\langle ., . \rangle$ is the regular inner product. The cost function for image reconstruction is defined as:

$$f(\vec{x}) = L(\vec{x}) + \beta T(\vec{x}), \tag{2}$$

where $L(\vec{x})$ is the negative log-likelihood function, $T(\vec{x})$ is a penalty function based on ℓ_0 norm and β is a hyperparameter defined as:

$$L(\vec{x}) = \sum_{i=1}^{m} \left[b_i \exp(-\langle \vec{a_i}, \vec{x} \rangle) + y_i \langle \vec{a_i}, \vec{x} \rangle \right], \tag{3}$$

$$T(\vec{x}) = \sum_{j=1}^{n} s(x_j), \quad s(t) = \lim_{\epsilon \to 0} |t|^\epsilon \equiv \begin{cases} 1 & t \neq 0 \\ 0 & t = 0 \end{cases}. \tag{4}$$

The formulation of the image reconstruction cost function in Eq. (2) can be simply indicate that, the reconstructed image is the most sparse image that fit with the measured projection data. This approach can successfully find the object support by threshold the image pixels that is close to zero to the value of zero. The minimization of cost function using the majorization-maximization approach [8] leads to the following iterative reconstruction algorithm:

1 Initialization $x^{(0)} = \epsilon$, with $\epsilon > 0$, $k \leftarrow 0$
repeat
  for $j = 1 : n$ **do**
2 $p_j = x_j^k + x_j^k \frac{\sum_i a_{ij} \left[b_i \exp(-\langle \vec{a_i}, \vec{x}^k \rangle) - y_i \right]}{\sum_i a_{ij} \langle \vec{a_i}, \vec{x}^k \rangle b_i \exp(-\langle \vec{a_i}, \vec{x}^k \rangle)}$
    $t_j = \frac{\sum_i a_{ij} \langle \vec{a_i}, \vec{x}^k \rangle b_i \exp(-\langle \vec{a_i}, \vec{x}^k \rangle)}{2\beta x_j^k}$
3 $x_j^{k+1} = \begin{cases} 0 & (p_j \leq \sqrt{1/t_j}) \\ p_j & (otherwise) \end{cases}$
  end
  $k \leftarrow k + 1$
until *stopping criterion*;

III. Experimental Results

In the experiment studies, we have used a three-dimensional high-resolution CT data obtained from a third-generation synchrotron radiation source located in Hyogo, Japan (SPring-8) [9].

A. Aluminum alloy data

In the first experiment, the object sample was a metallic Aluminum alloy (Al-Cu). In this imaging application, the air holes and the distribution of the alloy components are required to be observed in the sample. Two sets of data are used, the first one was acquired using sample of size $1mm$, which is completely fit inside the FOV to be used as a true reference for the later scan. The second dataset was acquired using a sample of size $2mm$ by including an external shield to the original sample imaged earlier. The data is acquired from BL20XU beamline with CCD of 2000×1312 that reconstructed in

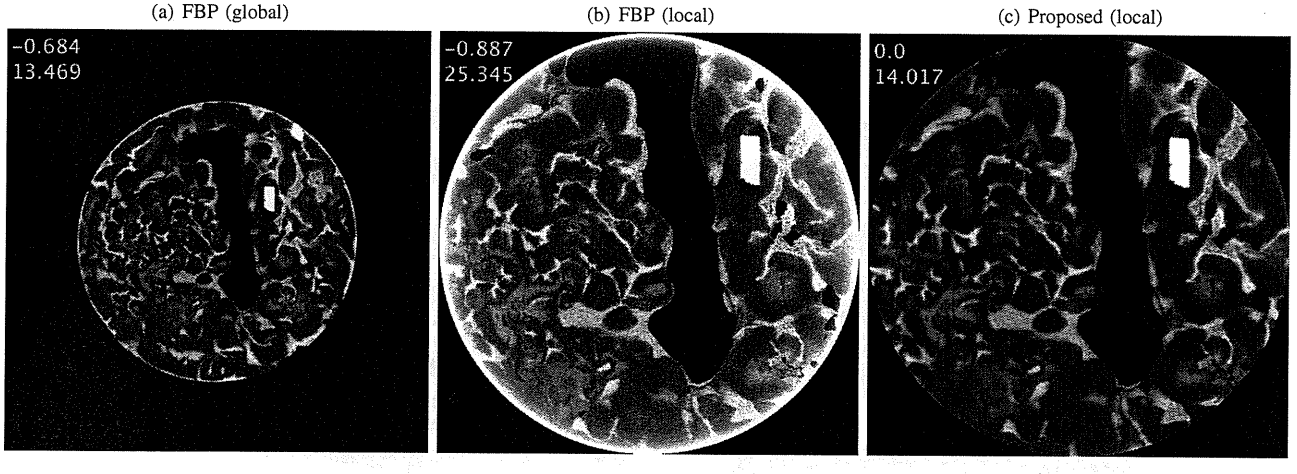

Fig. 3. Global image reconstructed from full projection data (left), local images reconstructed using standard FBP algorithm (middle), and ROI-OSEM algorithm (right). Intensity value ranges are displayed on top left corner of each images.

volume of size $2000 \times 2000 \times 1312$ with pixel size of $0.5\mu m$. The projection data was measured for 1500 views over 180° with energy of 35 keV. A single slice of the first dataset, which is not truncated, was reconstructed using FBP algorithm. The corresponding slice in the second dataset was reconstructed using FBP and proposed method. Results, shown in Fig. 2, indicate that the proposed method can reduce the DC-shift and low-frequency artifacts in the image reconstructed from local data.

B. Calcite in tarc

In this experiment, the object was a sample of tarc fluid containing calcite powder. In this application, it is required to investigate the internal structure of micro-size sample. The exact intensity value is important to identify the correct structure and any DC-shift occurs due to data truncation may lead to incorrect identification of the sample contents. Two sets of data, global and local, were acquired using an x-ray energy of 20 keV at BL20B2 beamline. The global data was obtained using a detector size of 1560×680 bins with bin size of 6.66 μm. In these settings the whole object was located completely inside the detector FOV and the projection data was computed over 2250 view angles over 180°. The local data was acquired with a magnification of the central region of the sample. The data was obtained using a detector of size 2000×1312 bins with bin size of 3.33 μm and 3000 view angels over 180°. Although, the local data provides a higher resolution (doubled) to the central region of the sample, the projection data was fully truncated and represents a local tomography.

The global data corresponding to central slice was used to reconstruct image of the whole object with 1560×1560 pixels using standard FBP algorithm, shown in Fig. 3(a) to be used as a reference for the evaluation of the proposed method. The local data of the central slice was used to reconstruct a magnified image of 2000×2000 pixels of an internal structure of the sample. The reconstruction using standard FBP and proposed method with 10 iterations are shown in Fig. 3. The proposed method succeeded in reducing the artifacts existing in the analytical reconstruction from local projection data. The correct estimation of the object support and the internal region, corresponding to air hole, lead to an exact local reconstruction.

C. Mouse lung

In this experiment, a real data acquired from a mouse, was used to investigate the structure of lung alveoli. The mouse was imaged BL20B2 beamline. The projection data was acquired using a detector of 2000×300 bins with bin size of 3.33 μm with a set of 1500 projection angles over 180°. The projection data was fully truncated such that the detector FOV was located completely inside the mouse. No information regarding the true object were measured during data acquisition. A single slice was reconstructed using standard FBP and the proposed method. The reconstructed images and the corresponding central horizontal and vertical profiles are shown in Fig. 4.

IV. Conclusion

In this work, we proposed statistical iterative reconstruction algorithm for local tomography. The proposed method is based on simple approach that effectively estimate the require *a priori* known information for accurate and stable reconstruction from fully truncated projection data. The proposed method is tested using SR micro-CT real data and effective achievement in image quality is observed compared to conventional methods. However, the computation cost of the proposed method still the major challenge. Future work include the reducing the computation cost to a reasonable level for practical implementation in high-resolution micro-CT imaging.

References

[1] F. Natterer, *The Mathematics of Computerized Tomography*, Philadelphia, PA: Wiley, 1986.

[2] F. Noo, R. Clackdoyle and J. D. Pack, "A two-step Hilbert transform method for 2D image reconstruction," *Phys. Med. Biol.*, vol. 49, pp. 3903-3923, 2004.

[3] M. Defrise, F. Noo, R. Clackdoyle and H. Kudo, "Truncated Hilbert transform and image reconstruction from limited tomographic data," *Inverse Problems*, vol. 22, pp. 1037-1053, 2006.

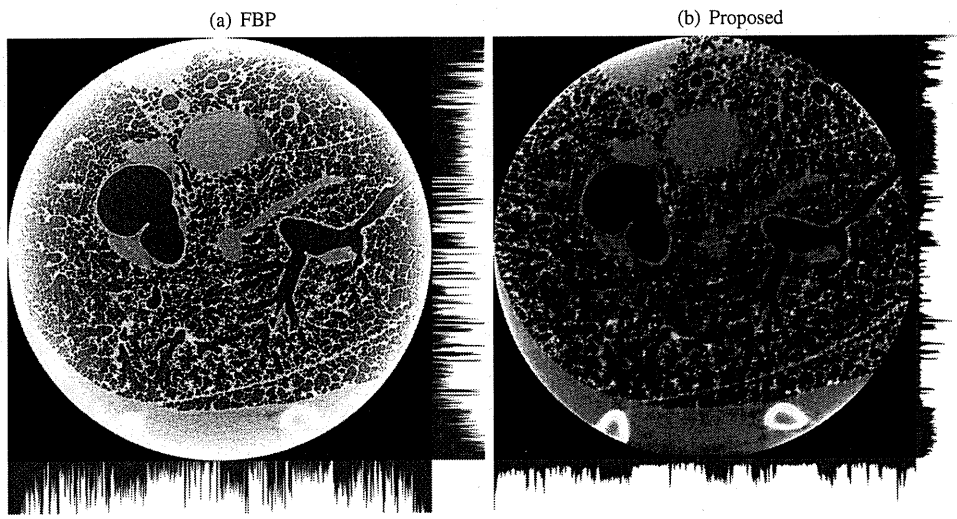

Fig. 4. Reconstructed images using FBP algorithm (left) with strong DC-shift and low-frequency artifacts and using the proposed iterative method (right) show a significant artifact reduction. Central horizontal and vertical profiles are also shown.

[4] H. Kudo, M.Courdurier, F.Noo and M.Defrise, "Tiny *a priori* knowledge solves the interior problem in computed tomography," *Phys. Med. Biol.*, vol. 53, pp. 2207-2231, 2008.
[5] X. Pan, Y. Zou and D. Xia, "Image reconstruction in peripheral and central regions-of-interest and data redundancy," *Med. Phys.*, vol. 32, pp. 673-684, 2005.
[6] E. Rashed and H. Kudo, "Region-of-Interest reconstruction from truncated projection data under blind object support", *Conference Record of 2008 IEEE Medical Imaging Conference*, Paper No. M03-7, 2008.
[7] Y. Ye, H. Yu, Y. Wei and G. Wang, "A general local reconstruction approach based on a truncated Hilbert transform," *Int. J. Biomed. Imaging*, vol. 2007, Article ID 63634 (8 pp), 2007.
[8] J. A. Fessler and A. O. Hero, "Penalized maximum-likelihood image reconstruction using space-alternating generalized EM algorithms," *IEEE Trans. Image Process.*, vol.4, pp. 1417-1429, 1995.
[9] http://www.spring8.or.jp

OPEN ACCESS Freely available online

PLoS one

Spatial Frequency-Based Analysis of Mean Red Blood Cell Speed in Single Microvessels: Investigation of Microvascular Perfusion in Rat Cerebral Cortex

Joonas Autio[1☯¤], Hiroshi Kawaguchi[1☯], Shigeyoshi Saito[1], Ichio Aoki[1], Takayuki Obata[1], Kazuto Masamoto[1,2], Iwao Kanno[1]*

1 Department of Biophysics, Molecular Imaging Center, National Institute of Radiological Sciences, Anagawa, Chiba, Japan, **2** Center for Frontier Science and Engineering, University of Electro-Communications, Chofu, Tokyo, Japan

Abstract

Background: Our previous study has shown that prenatal exposure to X-ray irradiation causes cerebral hypo-perfusion during the postnatal development of central nervous system (CNS). However, the source of the hypo-perfusion and its impact on the CNS development remains unclear. The present study developed an automatic analysis method to determine the mean red blood cell (RBC) speed through single microvessels imaged with two-photon microscopy in the cerebral cortex of rats prenatally exposed to X-ray irradiation (1.5 Gy).

Methodology/Principal Findings: We obtained a mean RBC speed (0.9±0.6 mm/sec) that ranged from 0.2 to 4.4 mm/sec from 121 vessels in the radiation-exposed rats, which was about 40% lower than that of normal rats that were not exposed. These results were then compared with the conventional method for monitoring microvascular perfusion using the arteriovenous transit time (AVTT) determined by tracking fluorescent markers. A significant increase in the AVTT was observed in the exposed rats (1.9±0.6 sec) as compared to the age-matched non-exposed rats (1.2±0.3 sec). The results indicate that parenchyma capillary blood velocity in the exposed rats was approximately 37% lower than in non-exposed rats.

Conclusions/Significance: The algorithm presented is simple and robust relative to monitoring individual RBC speeds, which is superior in terms of noise tolerance and computation time. The demonstrative results show that the method developed in this study for determining the mean RBC speed in the spatial frequency domain was consistent with the conventional transit time method.

Citation: Autio J, Kawaguchi H, Saito S, Aoki I, Obata T, et al. (2011) Spatial Frequency-Based Analysis of Mean Red Blood Cell Speed in Single Microvessels: Investigation of Microvascular Perfusion in Rat Cerebral Cortex. PLoS ONE 6(8): e24056. doi:10.1371/journal.pone.0024056

Editor: Timothy W. Secomb, University of Arizona, United States of America

Received February 16, 2011; **Accepted** August 3, 2011; **Published** August 24, 2011

Funding: The study was partly supported by the Scandinavia-Japan Sasakawa Foundation (JA), the Special Coordination Funds for Promoting Science and Technology (KM), and KAKENHI from Japan Society for the Promotion of Science in Japan (TO and HK). The funders had no role in study design, data collection and analysis, decision to publish, or preparation of the manuscript.

Competing Interests: The authors have declared that no competing interests exist.

* E-mail: kanno@nirs.go.jp

☯ These authors contributed equally to this work.

¤ Current address: Department of Neurobiology, A. I. Virtanen –Institute, University of Eastern Finland, Kuopio, Finland

Introduction

Prenatal exposure to X-ray irradiation is a leading cause of postnatal development deficits such as a decrease in brain size and retardation of behavioral and mental activity [1]. Recently, we found that X-ray irradiation exposure (1.5 Gy) on the 15th day of pregnancy impaired the development of vascular endothelial cells and cerebral arteriogenesis in postnatal rat brains [2]. Further, following prenatal exposure to irradiation, newborn rats showed reduced cerebral blood flow (CBF), which was only half of that observed in age-matched non-exposed rats [2]. These findings suggest that immature development of the brain vasculature, including cerebral hypo-perfusion, is of etiological importance in the delayed development of the central nervous system (CNS) observed in subjects following prenatal exposure to X-ray irradiation.

Because the CBF reflects a product of cortical blood volume per unit tissue volume and cross-sectional blood velocity in the vessels, the cerebral hypo-perfusion observed in the exposed subjects could be due to low blood volume (i.e., decrease in capillary density) in the parenchyma tissue relative to non-exposed subjects, or it could be due to a decrease in blood velocity through the parenchyma capillaries. In the former case, low blood volume may result from an immature development of the microvasculature. In the latter case, a decline in blood velocity can be interpreted as a higher resistance in the cerebral circulation in the exposed subjects, which can be attributed to a narrow lumen space of cerebral arteries or low demand of metabolic activity in parenchyma tissue. In either case, it is necessary to measure the blood velocity in the parenchyma capillaries directly to further determine the source of the hypo-perfusion observed in the prenatal exposed subjects.

Using a variety of fast-scanning optical microscopic techniques, previous studies have shown that the mean red blood cell (RBC) speed in cortical microvessels ranged from 0.4 to 1.5 mm/sec in anesthetized rats [3-7]. However, these studies were limited to microvessels located on the cortical surface, but not in parenchyma capillaries, where neural processes and metabolic activity occur. Alternatively, Kleinfeld et al. [8] first used two-photon microscopy to directly visualize RBC movement through the parenchyma capillaries up to a depth of 600 μm. Two-photon microscopy has an increase in the depth of tissue penetration into biological tissue as compared to other most commonly used optical microscopes [9,10]. The near-infrared excitation wavelengths used in two-photon microscopy allows for high penetration of the light into the tissue due to low absorption and scattering effects [11]. However, the depth penetration of two-photon imaging is decreased in circumstances of increased tissue absorption and scattering [12,13], which makes analyzing small targets, i.e., moving RBCs, difficult, such as in disease model animals where the scattering and/or absorption of light by the tissue is high.

To overcome the potential limitations in analyzing RBC speed from poor contrast-to-noise ratio images in disease model animals, we developed an analytical method based on a two-dimensional fast Fourier transform (FFT) approach. This method is similar to that used in a recent study by Drew et al. [14] who used the Radon transform to characterize the spatial pattern of the RBC traces. In their study, it was shown that a coordinate-transform method is superior in terms of noise tolerance for the extraction of RBC slope from line-scanned vascular images, as compared to the original approach with a singular value decomposition (SVD) method [8]. The 2D FFT approach presented here directly utilized raw line-scanned images, which contained vascular and non-vascular signals. The method was then applied to determine the mean RBC speed in the cerebral cortex in rats receiving prenatal X-ray irradiation (1.5 Gy) according to our previous study [2]. These results were further compared with the conventional method for determining the microvascular perfusion based on the arteriovenous transit time (AVTT) [15-17] in both X-ray exposed and non-exposed rats. Using this new analytical approach to determine the microvascular RBC speed and conventional AVTT measurements, we consistently found approximately 40% lower microvascular perfusion in the cerebral cortex of prenatally exposed rats as compared to non-exposed rats.

Results

RBC speed in single microvessels

Figure 1A shows a representative raw image of an RBC trace using the two-photon line-scanning method at a single location in the parenchyma microvessel. Dark streaks in the image represent the unlabelled RBC moving through the vessel in a longitudinal direction. Figure 1B shows a power spectrum image calculated from the 512 by 512 pixel image in Fig. 1A. The oblique shape in the FFT image is elongated in the direction perpendicular to the dark streaks in the original image. Changing to polar coordinates in the frequency space, the power spectrum was summed along lines of θ (Fig. 1C, and see Eq. 2). The angle corresponding to the peak of the radial spectrum was then used to calculate the mean RBC speed with Eq.1. The mean RBC speed in this representative image was calculated to be 1.1 mm/sec. Under our experimental protocol, the time required to compute the mean RBC speed was 0.60 sec per image with the proposed method, which was faster than a method employing SVD (4.74 sec per image), and almost equivalent to a method using the Radon transform (0.75 sec per image). The population data (121 vessels from four exposed rats) showed that the obtained mean RBC speed ranged from 0.2 to 4.4 mm/sec, and the mean of all measurements was 0.9±0.6 mm/sec (Fig. 2).

Cortical AVTT measurements

Figure 3A shows an image of the appearance time measured on the cortical surface of a representative non-exposed animal. Based on the spatial continuity of the appearance over time, arterial and venous segments were determined (37,638 and 97,272 pixels in this representative image, which accounted for 14% and 37% of

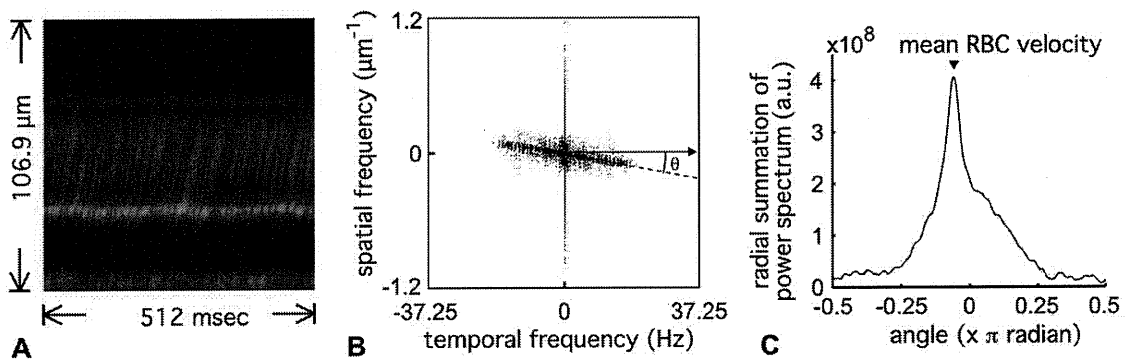

Figure 1. Representative image and measurement of RBC speed in single microvessels of the exposed animals. (A) A raw image of RBC moving through a microvessel was obtained using a line-scan mode with two-photon microscopy. The representative image showed 512 lines captured at the center of the target microvessel in parallel to the longitudinal direction. The x-axis represents Δt of 1 msec/pixel (time domain), and the y-axis is Δx of 0.20 μm/pixel (spatial domain). The green color represents the measured intensity of the fluorescent signal that originated from the injected plasma marker. Dark streaks observed around the center of the image were mainly caused by unlabelled RBC motions, and their slopes reflect a speed of the RBC motions that were parallel to the vessel length (a scan direction). (B) Power spectrum image. The image represents a FFT image constructed from the original 512 by 512 pixel image (A). The power spectrum was used to characterize a periodic pattern of the pixel intensity distribution represented in the raw image (A). A slanted line reflects a direction preference, perpendicular to the RBC traces (i.e., a slope of dark streaks), which appeared in the original image. The angle between this slanted line and the temporal axis was used to calculate the mean RBC speed (see text). (C) The spatial pattern of the pixel intensity distribution converted by the FFT analysis. Summation of the power spectrum at each angle was calculated for all directions (-0.5 to 0.5 π), and the angle that had the maximum power (arrow head) was used to calculate mean RBC speed (1.1 mm/sec in this representative image) (see Eq. 1).
doi:10.1371/journal.pone.0024056.g001

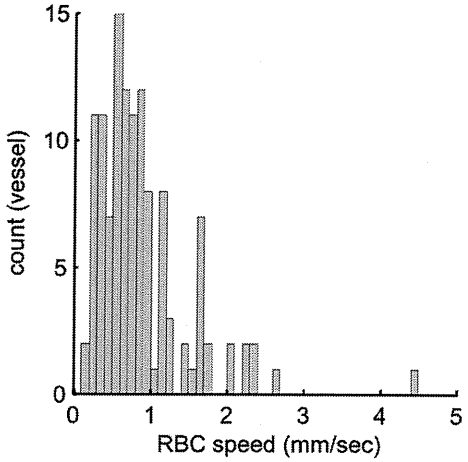

Figure 2. Mean RBC speed in single microvessels. The histogram shows the frequency distribution of the mean RBC speed obtained from all 121 vessels in the exposed rats (N = 4). The mean RBC speed ranged from 0.2 to 4.4 mm/sec (minimum to maximum), and the mean of all measurements was 0.9±0.6 mm/sec.
doi:10.1371/journal.pone.0024056.g002

total pixel numbers, respectively, Fig. 3B). In this rat, the mean appearance time was 0.29±0.28 and 1.43±0.48 sec in the arterial and venous segments, respectively (see Fig. 3C). Consequently, the AVTT was calculated as 1.14 sec. In addition, the median of the appearance time (0.21 and 1.33 sec in arterial and venous segments, respectively) was used to compare transit times. The AVTT was 1.12 sec, which was similar to the results obtained from the mean value. Therefore, the AVTT was calculated using the mean values.

A clear separation in the appearance time between the arterial and venous segments was consistently observed in all four exposed animals (Fig. 4A). The mean area of the observed vascular segments was 15,789±10,909 and 34,355±11,539 pixels in the arterial and venous segments, respectively, corresponding to 6±4% and 13±4% of the total number of pixels (262,144) in the image, respectively. In contrast, the results for the non-exposed animals were 12±4% and 30±9% of the pixels occupied by the arterial and venous segments, respectively. Interestingly, the mean ratio of the areas covered by the arterial and venous segments was similar for the exposed (1:2.2) and non-exposed (1:2.4) animals.

The mean of the AVTT was 1.9±0.6 sec in exposed animals, which was significantly longer than that of non-exposed animals (1.2±0.3 sec, Fig. 4B). To further compare the baseline capillary blood velocities in the exposed and non-exposed animals, the inverse of the mean AVTT was plotted in Figure 5B. Assuming that the tissue blood volume (i.e., a total vessel length) was the same for the two groups, the observed inverse transit times may reflect the mean of capillary blood speed through the parenchyma tissue. Comparison of the inverse transit times for the non-exposed and exposed groups found a ratio of 66%. A comparison for the mean capillary RBC speed measured in the present (exposed) and previous (non-exposed) studies found a similar ratio of 60% (Fig. 5A).

Discussion

Technical issues of frequency-based image analysis

Using the spatiotemporal frequency-based approach, the automated image analysis method was developed to measure the mean RBC speed from the population of RBCs moving in single microvessels of the cerebral cortex (Figs. 1, 2). The advantages of the present approach are the following: i) the mean RBC speed can be determined from images that contain a population of RBCs without distinguishing individual cells, such as for low signal-to-noise images, ii) the computation time required for the calculation is significantly improved relative to the previously-reported method with SVD, and iii) the algorithm is simple and no prior information is required, which makes it easy to implement. Based on a space-time image obtained by a line-scanning of RBC motions along the vessel, early studies have established a method that enabled RBC speed to be determined from the slope of the

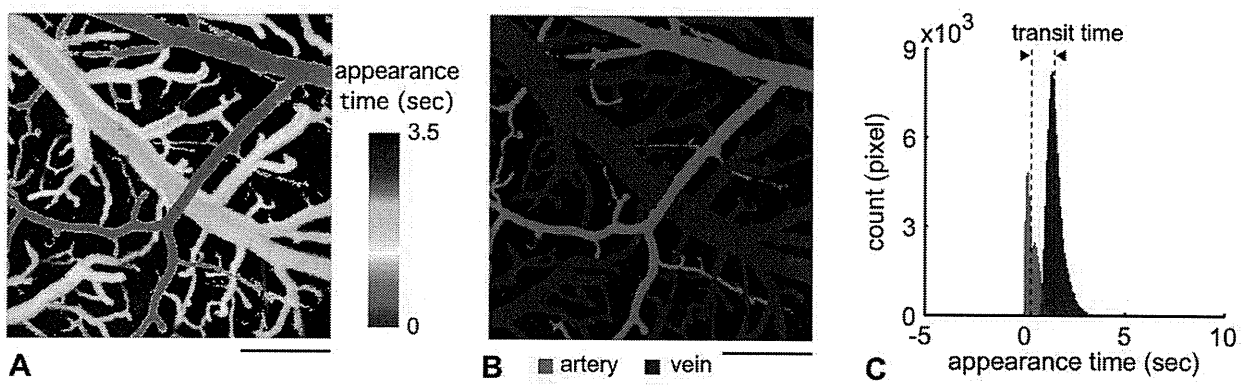

Figure 3. Representative image and measurement of AVTT. (A) A representative image of the appearance time obtained from one animal. Time-lapse imaging was performed at the cortical surface with a frame-capture rate of 14.2 frame/sec. The field of view was 512 by 512 pixels, and in-plane resolution was 3.6 μm/pixel. The pixel-basis analysis of appearance time was performed (see text). The image showed a continuity of appearance time in each vascular segment. An early appearance time (red) mostly represented an arterial flow, whereas a late appearance time (yellow to blue) resulted from venous flow. The color bar indicates the image acquisition time. Scale bar: 0.5 mm. (B) Segmentation of arterial and venous compartments. The arterial (red) and venous (blue) blood vessel areas were determined based on the spatial continuity of the appearance time observed along a longitudinal direction of the vessels (see text). Scale bar: 0.5 mm. (C) AVTT. The histogram represents the frequency distribution of appearance time observed in respective arterial (red) and venous (blue) areas. A total of 37,638 and 97,272 pixels were counted for arterial and venous segments, respectively, in this representative animal. Mean appearance time was observed as 0.29±0.28 and 1.43±0.48 sec in the arterial and venous segments, respectively, and thus, AVTT was 1.14 sec (a width between dashed vertical lines).
doi:10.1371/journal.pone.0024056.g003

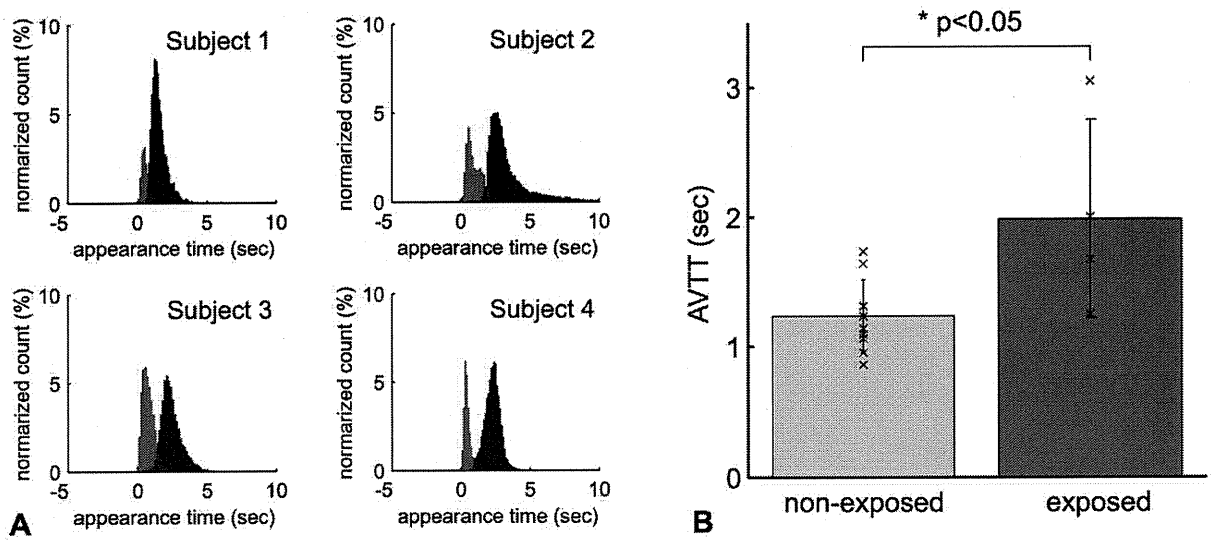

Figure 4. A comparison of mean AVTT. (A) The normalized histogram of the appearance time in all exposed rats (N = 4). The consistent distribution pattern of the appearance time was observed for both the arterial (red) and venous (blue) segments. (B) Population data on mean AVTT. Mean of AVTT was 1.2±0.3 and 1.9±0.6 sec in non-exposed (N = 9) and radiation exposed animals (N = 4), respectively. There were statistically significant differences between the two groups ($p<0.05$).
doi:10.1371/journal.pone.0024056.g004

RBC displacement per certain time intervals (i.e., scanning intervals) [4,17]. Later studies have presented a variety of image-based approaches, using SVD [8,18], two-dimensional image autocorrelation [19], Hough transform [20], and Radon transform [14,21], to extract the average slope. In particular, the SVD and Radon transform methods have been widely used to automatically determine dynamic changes in brain capillary RBC speeds [22-24]. For dynamic imaging, computation time is a key issue for achieving real time monitoring. We compared the computation time required for the method proposed in this paper and these alternative methods, and found that under our experimental conditions the proposed method is about 8 times faster than the SVD and equivalent to or slightly faster (1.25 times) than the Radon transform methods. With a Radon transform approach and simulated data degraded with various levels of noise, Drew et al. [14] showed that the coordinate-transform method has some advantages over the SVD. The 2D FFT presented here utilized the periodic pattern of the pixel intensity distribution (i.e., RBC streaks), and thus is relatively insensitive to signal arising from the non-vascular areas. This means that there is no need to crop the vascular areas from the raw image to detect RBC streaks. This is demonstrated in our supplementary results where it is shown that when the image covered relatively large non-vascular areas, the present method found a single unique peak, whereas the Radon

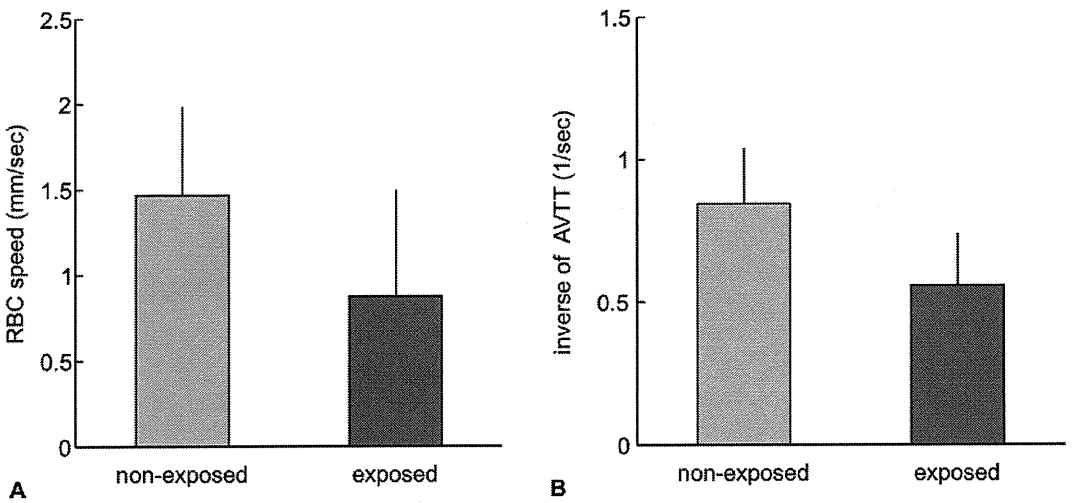

Figure 5. A comparison of capillary blood speeds. (A) Mean capillary RBC speed. The mean capillary RBC speed measured in the present study for the exposed animals (N = 4) was 40% lower than that for the non-exposed animals measured in a previous study (modified from [30]). (B) Inverse of the mean AVTT. The inverse of the mean AVTT of the exposed animals was 34% lower than that of the non-exposed animals. The ratio of exposed to non-exposed animal results was similar for both data sets.
doi:10.1371/journal.pone.0024056.g005

transform method did not (Fig. S1). An algorithm that reliably provides a unique peak is important for running the automated analysis, and no requirement to crop the images would be beneficial in reducing user bias and the number of steps in image processing. Further, specificity of the present method to the RBC streaks in the image could be used to reduce non-vascular signals by applying a bandpass filter in the frequency domain. This approach would be also useful as a pre-processing step (denoising) prior to identifying individual RBCs for counting [25], fitting [26], and tracking [27-29].

In contrast, one limitation of the frequency-based approach is that the method is only applicable to an image that contains a single pattern of RBC traces. If the images contain multiple patterns of RBC traces, such as due to temporal fluctuations and spatial variations of RBC movements through a single microvessel, it is necessary to assign an appropriate region of interest and time window (see also Fig. S2). The spatiotemporal dynamics of the RBC behaviors, such as during spontaneous fluctuations and response to neural functions in both prenatal exposed and non-exposed subjects, must be investigated in future studies.

Radiation effects on cerebral microcirculation

We observed that the mean RBC speed was 0.9±0.6 mm/sec in the exposed rats (Fig. 2), which was approximately 40% lower than that in isoflurane-anesthetized normal rats (Fig. S3 modified from [30]). Other studies have shown that the mean RBC speed in the microvessel on the cortical surface and parenchyma tissue ranged from 0.4 to 1.5 mm/sec as measured in anesthetized rats [3-8,22,31]. This large variation could be due to animal physiology from various labs and/or methods used to determine the RBC speed. In our previous study, we found that anesthesia significantly impacted the mean RBC speed in cortical microvessels; 0.4±0.4 mm/s and 1.5±0.4 mm/s under alpha-chloralose and isoflurane, respectively [30]. These findings are consistent with other reports that examined the anesthesia-dependence of CBF in rats [32,33]. The CBF in the somatosensory cortex of rats under isoflurane was shown to be equivalent to the non-anesthetized awake rats (130-150 ml/ 100g/ min) [34], indicating that isoflurane anesthesia is the preferred anesthetic to preserve normal CBF characteristics [35]. Using a high-speed confocal laser scanning microscope, it has been shown that the high-frame rate measurements (500 frame/s) recorded a 2.2 mm/s average for RBC speed (ranged from 0.8 to 6.6 mm/sec) in rats and mice [36,37]. Therefore, our RBC measurements were further compared with the conventional method for microvascular perfusion measurements [15,16]. In the present study, a fluorescent dye was injected into the femoral vein to measure the cortical AVTT. During its passage to the measurement site in the cortex the concentration of the dye will be diluted with blood, and this might complicate the separation of artery and venous segments. To avoid this possibility, we used the earliest image where the fluorescent signal appeared in a particular vessel for artery-vein segmentation (Fig. 3). Other studies have injected dye directly into the internal carotid artery [38,39], which allows the arrival of the dye at the imaging area of the cortex to be approximated by an impulse function (Dirac's delta). From preliminary tests with dye injection into the internal carotid artery, we found the mean AVTT to be 1.3±0.6 sec for the normal rats (N = 3), which was in good agreement with the present results (1.2±0.3 sec) obtained with dye injection into the femoral vein of the non-exposed rats. The intravenous injection is less-invasive than arterial injection methods, and thus has the advantage of permitting repeated long-term measurements of cerebral microvascular perfusion [40]. As a non-invasive technique, laser-Doppler flowmetry (LDF) might be considered as a good alternative to repeated long-term CBF measurements with a dye. However, LDF measures only relative changes with respect to the baseline CBF condition and thus may not be suitable for subject comparisons of stationary CBF between normal and disease states.

For the group comparisons, we assumed that blood volume per unit tissue was equivalent for the exposed and non-exposed animals. However, if the total vessel length is longer in the exposed rats, this might explain the longer mean AVTT that was observed. However, since our MR data showed that the cortical thickness in the exposed animals was only 36% of that of age-matched non-exposed animals (data not shown), this possibility can be ruled out. Measurements of the RBC speed and inverse of mean AVTT consistently showed an approximately 40% decline in cortical microvascular perfusion in the exposed rats in comparison to the non-exposed rats (Figs. 4, 5). These findings are also in good agreement with our previous measurements of CBF using magnetic resonance imaging (MRI) that showed that exposed newborn rats (postnatal 2 weeks) had approximately 50% of the CBF of the age-matched non-exposed rats [2].

The cerebral hypo-perfusion observed in the prenatal exposed rats could be due to the immature development of vascular systems and/or secondary effects of a lower energy demand in parenchyma tissue. In a previous study, with MR angiography, we found that the diameter of the middle cerebral artery was 63% smaller in the prenatally-exposed rats (0.24±0.02 mm) in comparison to the non-exposed age-matched animals (0.38±0.02 mm) [2]. In agreement with this finding, the present study showed that the area covered by arterial vessels on the cortical surface was almost half in the exposed animals relative to the non-exposed ones. Since the general physiology (MABP and heart rate) was not significantly different between the two groups, the possibility that the effects of radiation exposure on the CBF are due to general ill-health or lower cardiac output in the animals can be ruled out. Previous and present findings indicate that shrinkage of the major cerebral arteries could increase vessel resistance and result in parenchymal hypo-perfusion. Further technical improvement of cerebro-microvascular angiography would help highlight the main source of increased resistance at a microscopic scale.

In addition, no leakage of the fluorescent marker into the extravascular space was observed (data not shown), which indicates an intact blood-brain barrier (BBB) for the exposed as well as non-exposed animals. In a previous study, albumin-staining histology was performed to check the permeability of the BBB for prenatally-exposed rats [2]. The results showed that the number of albumin-positive cells in the cortex drastically decreased 2 weeks after birth for both exposed and non-exposed animals [2]. The findings also indicate that the function of the vascular endothelium (i.e., BBB permeability) developed normally for the prenatally exposed animal brains. In contrast, other studies have shown that X-ray exposure (60 Gy) of adult rats provoked disruption of BBB functions [41]. The discrepancy between the present and previous studies could be due to different dosage (1.5 Gy vs. 60 Gy) and/or age of exposure (prenatal vs. adult). In our studies, we also found that the mean density of laminin-positive cells (i.e., vascular endothelium cells) was significantly lower for the exposed (3,300 cells/mm^2) relative to the non-exposed (5,200 cells/mm^2) 2-week-old rat cortex [2]. The findings are consistent with results for adult rats and mice showing that loss of endothelial cells depends on X-ray irradiation dose and time after exposure [42,43]. Because the vascular endothelial cells belong to a category of high radiosensitivity cells [44], these observations suggest that prenatal exposure to X-ray irradiation damaged the development of vascular endothelial cells. A lack of endothelium development may further

disrupt the organization of CNS cells and networks. In this vein, an improvement or enhancement of endothelial cell growth potentially improves CNS cell development and neural connections, which may be a possible therapeutic target to prevent development defects in the prenatal exposed subjects. On the other hand, it has been shown that a density of cortical neurons and astroglia was preserved in the postnatal rats following X-ray irradiation (1.0 Gy) despite a decrease in cortical thickness [45,46]. These findings suggest that the local energy demand per unit volume was similar to that of non-exposed subjects. However, the total number of CNS cells decreased [45], and thus, the total energy level may be suppressed in exposed-animals. In this case, hypo-perfusion could result from a low metabolic demand in parenchyma tissue, which may be coupled to a total vascular length. Overall, these results strongly suggest that immature development of the brain vascular system and the related cerebral hypo-perfusion is of etiological importance in the delayed CNS development in subjects following prenatal exposure to X-ray irradiation. Future studies must address the molecular mechanism of CNS hypo-perfusion and its role in developing brains.

Conclusion

In conclusion, the present study developed a novel analytical method to determine the mean RBC speed from a large number of traces from a population of RBC images based on the 2D FFT approach. The method is simple and robust and enables automated quantification with minimum computation time. Further, the present study showed the significant decline in microvascular perfusion in the cerebral cortex of prenatal-exposed rats. These findings are consistent with our previous report [2]. Thus, the present method is valuable to further our understanding of the causal relationship between the decline of cerebral microvascular perfusion and delayed CNS development in the subjects following prenatal exposure to X-ray irradiation.

Materials and Methods

Animal preparation

The study was carried out in accordance with the recommendations in the Guide for the Care and Humane Use of Laboratory Animals of the National Institutes of Health. All experimental protocols were approved by the Institutional Animal Welfare Committee (Permit Number: 09-1008-4). In accordance with a previous study [2], two pregnant female Sprague-Dawley rats (15th day of pregnancy, Japan SLC, Hamamatsu, Japan) were irradiated with a single whole-body X-ray at a dose of 1.5 Gy (200 kVp, 20 mA, 0.5 mm Cu plus 0.5 mm Al filter). At eight to nine weeks after birth, a total of four male rats (230 to 300 g) from each breed were used for the experiments. Nine age-matched male Sprague-Dawley rats (210 to 320 g, Japan SLC, Hamamatsu, Japan) were also used as the non-exposed control group for microvascular AVTT measurements in the cerebral cortex.

The animals were anesthetized with isoflurane, and endotracheal intubation was performed to allow for mechanical ventilation. Catheters were placed into the femoral vein and artery for drug administration and for arterial blood sampling and monitoring systemic arterial blood pressure, respectively. The animal head was then fixed with stereotaxic frame (SG-3N, Narishige, Tokyo, Japan) by holding the animal nose and ears. Three needles were placed into the both sides of underarm and back for electrocardiogram (ECG) recording, and rectal temperature was maintained at 37°C. The left side of the skull over the somatosensory cortex (3 mm by 5 mm) was thinned with a dental drill. After the surgery was completed, the inspired gas was switched to a mixture of air and O_2 (30 to 35% total O_2), and the end-tidal isoflurane concentration was adjusted to 1.4%. The respiratory parameter was adjusted based on the arterial blood gas conditions: pH = 7.554±0.041, $PaCO_2$ = 32.3±1.0 mmHg, PaO_2 = 161±7 mmHg, hematocrit = 38.5±2.5%, and glucose concentration = 174±11 mg/dl in exposed group (N = 4), and pH = 7.471±0.024, $PaCO_2$ = 34.6±2.8 mmHg, PaO_2 = 136± 23 mmHg, hematocrit = 38.7±2.2%, and glucose concentration = 208±31 mg/dl in non-exposed group (N = 9). There were significant differences in the conditions of blood pH, PaO_2, and glucose concentrations between the exposed and non-exposed groups ($p<0.05$). Arterial blood pressure, measured with a blood pressure transducer (TSD104A, Biopac Systems, Inc., Goleta, CA), and heart rate, measured with an EEG amplifier (EEG100C, Biopac Systems, Inc.), were recorded throughout the experiments with a data acquisition system (MP150, Biopac Systems, Inc.) at a sampling rate of 100 Hz: mean arterial blood pressure (MABP) = 106±11 and 99±7 mmHg, and heart rate = 335±47 and 333±24 beats/min in exposed and non-exposed groups, respectively.

Measurement of microvascular RBC speed

The cortical microvasculature was imaged through a thinned skull using a two-photon laser scanning fluorescent microscope (TCS SP5MP, Leica Microsystems GmbH, Wetzlar, Germany) at 900-nm excitation (Mai Tai HP, Spectra-Physics, Santa Clara, CA) with an emission band-pass filter of 655/50 nm. Qdot 655 (1 μM in saline, Invitrogen, San Diego, CA) was intravenously injected into the animal to fluorescently label blood plasma [30]. RBC speed was measured in microvessels that had a diameter of less than 6 μm (i.e., capillaries) and a straight section at least 50 μm long, located between a depth of 50 and 300 μm from the cortical surface. For each target vessel, line scanning was repeatedly performed along the length of the vessel at a rate of 1-4 lines/ms, and a total of 512 lines were used to make a single image (i.e., 512 by 512 pixels, see also Fig. 1A). The image consists of an x-axis as the time domain (0.25-1 ms/pixel, Δt) and y-axis as the spatial domain (0.06-0.20 μm/pixel, Δx). The field of view and line-scan average were manually adjusted (i.e., 2-8 scan averages were typically performed with a scan speed of 0.125 ms/line). By setting 512 pixels along the horizontal axis (Δt), the temporal window was accordingly 128-512 ms, which allowed accurate calculation of the RBC speed under our experimental conditions. However, the window size is not limited. Depending on the line-scan average, an even shorter time-window (e.g., 32 pixels) is also possible (Fig. S2).

Mean RBC speed (v) was determined with the following equations:

$$v = |\mathbf{v}| = \left|\frac{\Delta x}{\Delta t}\cot\theta\right|, \quad (1)$$

where θ is the angle between the temporal frequency axis and a line perpendicular to the streaks (see Fig. 1B), and Δx and Δt are the spatial and temporal sampling intervals (i.e., a pixel width), respectively. Since Δx and Δt in Eq. (1) are given by the image acquisition parameters, θ is the only quantity that directly reflects the RBC speed. The angle θ was automatically calculated by detecting the angle having the maximum summation (g) of the power spectrum across all directions (from -0.5π to $+0.5\pi$) with a resolution of $\pi/180$ around a center of the frequency space (see Fig. 1C):

$$g(\theta) = \max_{\theta\in(-0.5\pi,0.5\pi)} \int_0^R F(r,\theta)dr, \quad (2)$$

where F(r, θ) is the transformation of a power spectrum image from Cartesian to polar coordinates. Two-dimensional linear interpolation was applied in the coordinate transformation. R was half of the pixel number, 255 in this study.

Measurement of the AVTT

Time-lapse imaging of the cortical surface vasculature was performed at a rate of 7.1, 9.5, or 14.2 frame/sec using a single-photon excitation mode (488-nm Argon laser). The image was 512 by 512 pixels, and the in-plane resolution was 3.6 μm/pixel. Immediately after the initiation of time-lapse imaging (within 10 sec), a bolus injection of Qdot 655 (1 ml/kg body weight) was administered in the femoral vein. AVTT was determined by imaging plasma markers but not RBC. Because negligible differences in the AVTT were observed between the plasma and RBC markers (data not shown), the equivalent flow characteristics of the plasma and RBC were assumed in the experimental conditions in the comparison of the measured RBC speed using conventional microvascular perfusion measurements. A median filter was first applied to reduce the shot noise of the detector (photomultiplier). AVTT was then calculated by subtracting the appearance time of the fluorescent signals determined at venous segments by those of arterial segments. The appearance time is the earliest time point that both target pixel intensity and the subsequent five time-point intensities surpassed a threshold level (i.e., mean + 2 S.D. of pre-injection baseline intensity). The baseline intensity was calculated by averaging all intensities measured during the pre-injection periods on a single pixel basis. If there were no time-points that surpass the threshold, that pixel was excluded from further analysis. Finally, arterial and venous segments were manually extracted based on a spatial continuity of the measured appearance time along a longitudinal direction of the vessels, and the appearance time of each segment was reported by averaging all pixel data of the respective segments. Data were presented as mean±S.D. across the animals unless otherwise specified, and a Student's t-test was performed for statistical analysis to compare the radiation-exposed and non-radiation group data.

Supporting Information

Figure S1 Comparison of with and without cropping for RBC speed estimation. (A) Raw image (512 by 512 pixels) captured by line scanning along a single vessel. The regions of interest in blue (cropped,128 by 128 pixels) and pink (non cropped, 512 by 128 pixels) were compared. (B) FFT. A single peak was consistently seen for both the cropped (blue) and non-cropped (pink) images. (C) Radon transform. Identical peak location was observed for the cropped (blue) and non-cropped (pink) images, but in the latter case the peak height was hidden by the components originating from non-vascular areas of the non-cropped image.
(PDF)

Figure S2 Temporal window and estimated RBC speeds. The dependence of RBC speed estimation on temporal window size was compared for the FFT and Radon transform methods. For less than 32 pixels (x-axis), both methods produced large variations away from the expected velocities (1 mm/s). Thus, a minimum of 32 pixels was needed to achieve accurate estimation. Note that the time window dependencies were similar for both the FFT and Radon transform methods.
(PDF)

Figure S3 RBC speed histogram for the non-exposed animals (modified from [30]). The RBC speed was directly measured by tracking the displacement of individual RBCs in the non-exposed rats [30] under similar experimental conditions to the present study. A mean speed of 1.5±0.4 mm/s was observed.
(PDF)

Acknowledgments

The authors thank Dr. Jeffrey Kershaw for proof reading.

Author Contributions

Conceived and designed the experiments: JA HK IA TO KM IK. Performed the experiments: JA HK SS KM. Analyzed the data: JA HK KM. Contributed reagents/materials/analysis tools: SS IA TO KM. Wrote the paper: JA HK KM IK.

References

1. Kimler BF (1998) Prenatal irradiation: a major concern for the developing brain. Int J Radiat Biol 73: 423–434.
2. Saito S, Aoki I, Sawada K, Sun XZ, Chuang KH, et al. (2011) Quantitative and noninvasive assessment of prenatal X-ray-induced CNS abnormalities using magnetic resonance imaging. Radiat Res 175: 1–9.
3. Ma YP, Koo A, Kwan HC, Cheng KK (1974) On-line measurement of the dynamic velocity of erythrocytes in the cerebral microvessels in the rat. Microvasc Res 8: 1–13.
4. Villringer A, Them A, Lindauer U, Einhäupl K, Dirnagl U (1994) Capillary perfusion of the rat brain cortex. An in vivo confocal microscopy study. Circ Res 75: 55–62.
5. Hudetz AG, Fehér G, Weigle CG, Knuese DE, Kampine JP (1995) Video microscopy of cerebrocortical capillary flow: response to hypotension and intracranial hypertension. Am J Physiol 268: H2202–H2210.
6. Seylaz J, Charbonné R, Nanri K, Von Euw D, Borredon J, et al. (1999) Dynamic in vivo measurement of erythrocyte velocity and flow in capillaries and of microvessel diameter in the rat brain by confocal laser microscopy. J Cereb Blood Flow Metab 19: 863–870.
7. Schulte ML, Wood JD, Hudetz AG (2003) Cortical electrical stimulation alters erythrocyte perfusion pattern in the cerebral capillary network of the rat. Brain Res 963: 81–92.
8. Kleinfeld D, Mitra PP, Helmchen F, Denk W (1998) Fluctuations and stimulus-induced changes in blood flow observed in individual capillaries in layers 2 through 4 of rat neocortex. Proc Natl Acad Sci U S A 95: 15741–15746.
9. Denk W, Strickler JH, Webb WW (1990) Two-photon laser scanning fluorescence microscopy. Science 248: 73–76.
10. Helmchen F, Denk W (2005) Deep tissue two-photon microscopy. Nat Methods 2: 932–940.
11. Kobat D, Durst ME, Nishimura N, Wong AW, Schaffer CB, et al. (2009) Deep tissue multiphoton microscopy using longer wavelength excitation. Opt Express 17: 13354–13364.
12. Dunn AK, Wallace VP, Coleno M, Berns MW, Tromberg BJ (2000) Influence of optical properties on two-photon fluorescence imaging in turbid samples. Appl Opt 39: 1194–1201.
13. Ying J, Liu F, Alfano RR (2000) Effect of scattering on nonlinear optical scanning microscopy imaging of highly scattering media. Appl Opt 39: 509–514.
14. Drew PJ, Blinder P, Cauwenberghs G, Shih AY, Kleinfeld D (2010) Rapid determination of particle velocity from space-time images using the Radon transform. J Comput Neurosci 29: 5–11.
15. Rovainen CM, Woolsey TA, Blocher NC, Wang DB, Robinson OF (1993) Blood flow in single surface arterioles and venules on the mouse somatosensory cortex measured with videomicroscopy, fluorescent dextrans, nonoccluding fluorescent beads, and computer-assisted image analysis. J Cereb Blood Flow Metab 13: 359–371.
16. Beck J, Stummer W, Lehmberg J, Baethmann A, Uhl E (2007) Arteriovenous transit time as a measure for microvascular perfusion in cerebral ischemia and reperfusion. Neurosurgery 61: 826–833.
17. Ellis CG, Ellsworth ML, Pittman RN, Burgess WL (1992) Application of image analysis for evaluation of red blood cell dynamics in capillaries. Microvasc Res 44: 214–225.
18. Schaffer CB, Friedman B, Nishimura N, Schroeder LF, Tsai PS, et al. (2006) Two-photon imaging of cortical surface microvessels reveals a robust redistribution in blood flow after vascular occlusion. PLoS Biol 4: e22.
19. Zipfel WR, Williams RM, Webb WW (2003) Nonlinear magic: multiphoton microscopy in the biosciences. Nat Biotechnol 21: 1369–1377.

20. Dobbe JG, Streekstra GJ, Atasever B, van Zijderveld R, Ince C (2008) Measurement of functional microcirculatory geometry and velocity distributions using automated image analysis. Med Biol Eng Comput 46: 659–670.
21. Duncan DD, Lemaillet P, Ibrahim M, Nguyen QD, Hiller M, et al. (2010) Absolute blood velocity measured with a modified fundus camera. J Biomed Opt 15: 056014.
22. Stefanovic B, Hutchinson E, Yakovleva V, Schram V, Russell JT, et al. (2008) Functional reactivity of cerebral capillaries. J Cereb Blood Flow Metab 28: 961–972.
23. Petzold GC, Albeanu DF, Sato TF, Murthy VN (2008) Coupling of neural activity to blood flow in olfactory glomeruli is mediated by astrocytic pathways. Neuron 58: 897–910.
24. Drew PJ, Shih AY, Driscoll JD, Knutsen PM, Blinder P, et al. (2010) Chronic optical access through a polished and reinforced thinned skull. Nat Methods 7: 981–984.
25. Hirase H, Creso J, Buzsáki G (2004) Capillary level imaging of local cerebral blood flow in bicuculline-induced epileptic foci. Neuroscience 128: 209–216.
26. Zhang S, Boyd J, Delaney K, Murphy TH (2005) Rapid reversible changes in dendritic spine structure in vivo gated by the degree of ischemia. J Neurosci 25: 5333–5338.
27. Chaigneau E, Oheim M, Audinat E, Charpak S (2003) Two-photon imaging of capillary blood flow in olfactory bulb glomeruli. Proc Natl Acad Sci U S A 100: 13081–13086.
28. Japee SA, Pittman RN, Ellis CG (2005) Automated method for tracking individual red blood cells within capillaries to compute velocity and oxygen saturation. Microcirculation 12: 507–515.
29. Malone MH, Sciaky N, Stalheim L, Hahn KM, Linney E, et al. (2007) Laser-scanning velocimetry: a confocal microscopy method for quantitative measurement of cardiovascular performance in zebrafish embryos and larvae. BMC Biotechnol 7: 40.
30. Masamoto K, Obata T, Kanno I (2010) Intracortical microcirculatory change induced by anesthesia in rat somatosensory cortex. Adv Exp Med Biol 662: 57–61.
31. Hutchinson EB, Stefanovic B, Koretsky AP, Silva AC (2006) Spatial flow-volume dissociation of the cerebral microcirculatory response to mild hypercapnia. Neuroimage 32: 520–530.
32. Hendrich KS, Kochanek PM, Melick JA, Schiding JK, Statler KD, et al. (2001) Cerebral perfusion during anesthesia with fentanyl, isoflurane, or pentobarbital in normal rats studied by arterial spin-labeled MRI. Magn Reson Med 46: 202–206.
33. Masamoto K, Kim T, Fukuda M, Wang P, Kim SG (2007) Relationship between neural, vascular, and BOLD signals in isoflurane-anesthetized rat somatosensory cortex. Cereb Cortex 17: 942–950.
34. Mackawa T, Tommasino C, Shapiro HM, Keifer-Goodman J, Kohlenberger RW (1986) Local cerebral blood flow and glucose utilization during isoflurane anesthesia in the rat. Anesthesiology 65: 144–151.
35. Hudetz AG, Lee JG, Smith JJ, Bosnjak ZJ, Kampine JP (1994) Effects of volatile anesthetics on cerebrocortical laser Doppler flow: hyperemia, autoregulation, carbon dioxide response, flow oscillations, and role of nitric oxide. Adv Pharmacol 31: 577–593.
36. Tomita M, Osada T, Schiszler I, Tomita Y, Unekawa M, et al. (2008) Automated method for tracking vast numbers of FITC-labeled RBCs in microvessels of rat brain in vivo using a high-speed confocal microscope system. Microcirculation 15: 163–174.
37. Unekawa M, Tomita M, Tomita Y, Toriumi H, Miyaki K, Suzuki N (2010) RBC velocities in single capillaries of mouse and rat brains are the same, despite 10-fold difference in body size. Brain Res 1320: 69–73.
38. Schiszler I, Tomita M, Fukuuchi Y, Tanahashi N, Inoue K (2000) New optical method for analyzing cortical blood flow heterogeneity in small animals: validation of the method. Am J Physiol Heart Circ Physiol 279: H1291–H1298.
39. Tomita Y, Tomita M, Schiszler I, Amano T, Tanahashi N, et al. (2002) Moment analysis of microflow histogram in focal ischemic lesion to evaluate microvascular derangement after small pial arterial occlusion in rats. J Cereb Blood Flow Metab 22: 663–669.
40. Tomita Y, Pinard E, Tran-Dinh A, Schiszler I, Kubis N, et al. (2011) Long-term, repeated measurements of mouse cortical microflow at the same region of interest with high spatial resolution. Brain Res 1372: 59–69.
41. Rubin P, Gash DM, Hansen JT, Nelson DF, Williams JP (1994) Disruption of the blood-brain barrier as the primary effect of CNS irradiation. Radiother Oncol 31: 51–60.
42. Ljubimova NV, Levitman MK, Plotnikova ED, Eidus LKh (1991) Endothelial cell population dynamics in rat brain after local irradiation. Br J Radiol 64: 934–940.
43. Peña LA, Fuks Z, Kolesnick RN (2000) Radiation-induced apoptosis of endothelial cells in the murine central nervous system: protection by fibroblast growth factor and sphingomyelinase deficiency. Cancer Res 60: 321–327.
44. Baker DG, Krochak RJ (1989) The response of the microvascular system to radiation: a review. Cancer Invest 7: 287–294.
45. Miki T, Fukui Y, Takeuchi Y, Itoh M (1995) A quantitative study of the effects of prenatal X-irradiation on the development of cerebral cortex in rats. Neurosci Res 23: 241–247.
46. Miki T, Yokoyama T, Sumitani K, Wang ZY, Yang W, et al. (2007) The effect of prenatal X-irradiation on the developing cerebral cortex of rats. II: A quantitative assessment of glial cells in the somatosensory cortex. Int J Dev Neurosci 25: 293–297.

《3》
機能情報における画像診断
《3-2》
SPECT画像を用いた認知症の計算機支援診断

工藤博幸†

キーワード　認知症，SPECT，計算機支援診断，画像処理，脳血流

1 まえがき

SPECT (Single Photon Emission CT) は，血流や代謝などの生体機能を映像化する医用画像診断装置で，特に重要な用途として，心臓病と脳疾患の画像診断に広く用いられている．類似の装置として，より高画質の画像を提供するPET (Positron Emission Tomography) が存在するが，PET装置は高価で多くの病院に導入されるには至っておらず，一般の病院では，機能画像を用いる診断にはSPECTが使われるのが現状である．

SPECTの原理を図1に示す．まず，放射性同位元素で標識した薬剤を体内に投与すると，薬剤は体内に分布して単光子と呼ばれるγ線光子を発生する．この光子を，体外に配置した，ガンマカメラと呼ばれる検出器で検出して，CTと同じ投影データを測定する．投影データの測定は，ガンマカメラを回転させて360°の角度範囲から行い，投影データにCTと類似した画像再構成のデータ処理を施して，薬剤の分布を画像化する．薬剤の種類を変えることで，さまざまな生体の機能を画像化できる．例えば，心筋の検査には，Tc-99m，Tl-201などの薬剤がよく用いられ，脳血流の検査には，I-123などがよく用いられる．

近年，認知症の患者数が急速に増加して社会問題になっていることを背景として，SPECTを用いた認知症の画像診断が注目されている．認知症の画像診断の手法としては，MRIで撮影した形態画像から脳萎縮を発見する手法と，SPECTで撮影した脳血流画像から血流低下を発見する手法がある．多くの場合，認知症では脳血流の低下がしばらく続いた後に脳萎縮が生じるため，SPECTにより，MRIで異常が現れるより早期の段階で診断を行うことが可能となる．したがって多くの病院では，認知症の診断にMRI画像とSPECT画像を併用しているのが現状である．しかし，病気初期段階においてSPECT画像に現れる血流低下は微少であり，医師の目視による画像の読影では不充分な場合が多く，最近は機能画像を解析するソフトウェアをセカンドオピニオンとして用いるのが一般的になってきた．

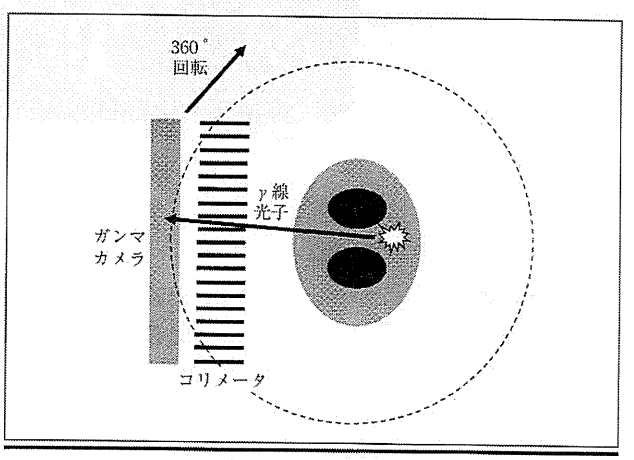

図1　SPECTの原理

この目的に用いられる画像解析のソフトウェアとしては，Fristonらが開発したSPM (Statistical Parameter Mapping) とMinoshimaらが開発した3D-SSP (3D Stereotactic Surface Projection) が有名で，実用化が進んでいる[1)〜4)]．いずれも1990年代に開発されたソフトウェアで，患者と健常者のSPECT画像を統計的に比較する原理に基づいており，統計学的画像解析法とも呼ばれる．一方，2005年に筆者らは，統計学的画像解析法とはまったく異なる新しい考え方の画像解析手法FUSE (Fuse SPECT and MRI) を提唱して，そのポテンシャルを示した[5)6)]．FUSEは，基礎実験を終了して企業と連携して，臨床評価とソフトウェア化を進めている段階である．機能画像を対象とした計算機支援診断は，X線画像やCTを対象としたものより遅れているのが現状であるが，その中で早くから研究が行われ，いち早く実用化されたのが，上述の脳血流SPECT画像の解析と言えるであろう．本論文では，認知症の診断を目的とした脳血流SPECT画像の解析を取り上げ，統計学的画像解析法とFUSEについて専門以外の方を対象として平易に解説する．

† 筑波大学 大学院システム情報工学研究科 コンピュータサイエンス専攻
"Computer-Aided-Diagnosis of Dementia Using SPECT Images" by Hiroyuki Kudo (Department of Computer Science, Graduate School of Systems and Information Engineering, University of Tsukuba, Tsukuba)

映像情報メディア学会誌 Vol. 65, No. 4, pp. 444〜447 (2011)